Title

Genomic Decoding of Neuronal Depolarization by Stimulus-Specific NPAS4 Heterodimers

Journal

Cell, 179(2)

ISSN

0092-8674

Authors

Brigidi, G Stefano

Hayes, Michael GB

Santos, Nathaniel P Delos

et al.

Publication Date

2019-10-01

DOI

10.1016/j.cell.2019.09.004

Peer reviewed

Published in final edited form as:

Cell. 2019 October 03; 179(2): 373–391.e27. doi:10.1016/j.cell.2019.09.004.

Genomic decoding of neuronal depolarization by stimulus-specific NPAS4 heterodimers

G. Stefano Brigidi[1], **Michael G. B. Hayes**[2], **Nathaniel P. Delos Santos**[2,3], **Andrea L. Hartzell**[1,4], **Lorane Texari**[2], **Pei-Ann Lin**[1,4], **Anna Bartlett**[5], **Joseph R. Ecker**[5,6], **Christopher Benner**[2], **Sven Heinz**[2], **Brenda L. Bloodgood**[1,*]

[1]Division of Biological Sciences, Section of Neurobiology

[2]Department of Medicine

[3]Department of Biomedical Informatics

[4]Neuroscience Graduate Program, University of California San Diego, 9500 Gilman Drive, La Jolla, CA, 92093-0634; USA

[5]Genomic Analysis Laboratory, The Salk Institute for Biological Studies, 10010 N Torrey Pines Road, La Jolla, CA, 92037; USA

[6]Howard Hughes Medical Institute

SUMMARY:

Cells regulate gene expression in response to salient external stimuli. In neurons, depolarization leads to the expression of inducible transcription factors (ITFs) that direct subsequent gene regulation. Depolarization encodes both a neuron's action potential (AP) output and synaptic inputs, via excitatory postsynaptic potentials (EPSPs). However, it is unclear if distinct types of electrical activity can be transformed by an ITF into distinct modes of genomic regulation. Here, we show that APs and EPSPs in mouse hippocampal neurons trigger two spatially segregated and molecularly distinct induction mechanisms that lead to the expression of the ITF NPAS4. These two pathways culminate in the formation of stimulus-specific NPAS4 heterodimers that exhibit distinct DNA binding patterns. Thus, NPAS4 differentially communicates increases in a neuron's spiking output and synaptic inputs to the nucleus, enabling gene regulation to be tailored to the type of depolarizing activity along the somato-dendritic axis of a neuron.

[*]Lead Contact and Correspondence addressed to: Brenda L. Bloodgood, Ph.D.

AUTHOR CONTRIBUTIONS

G.S.B. and B.L.B. conceived of the study, designed the experiments, and co-wrote the manuscript. G.S.B. performed electrophysiology, immunohistochemistry, *in situ* hybridization, biochemistry, and ChIP- and RNA-seq experiments, conducted data analysis, and assembled figures. M.G.B.H. conducted ChIP-seq experiments and analysis. N.P.D.S performed ChIP- and RNA-seq analysis. A.L.H. performed electrophysiology, immunohistochemistry, and data analysis. P-A.L. performed immunohistochemistry and data analysis. L.T. contributed methodological assistance with ChIP-seq, and conducted analysis. A.B. and J.R.E. assisted with sequencing analysis. S.H. and C.B. designed and supervised ChIP-seq experiments and analysis.

DECLARATION OF INTERESTS

The authors declare no competing financial interests.

Graphical Abstract:

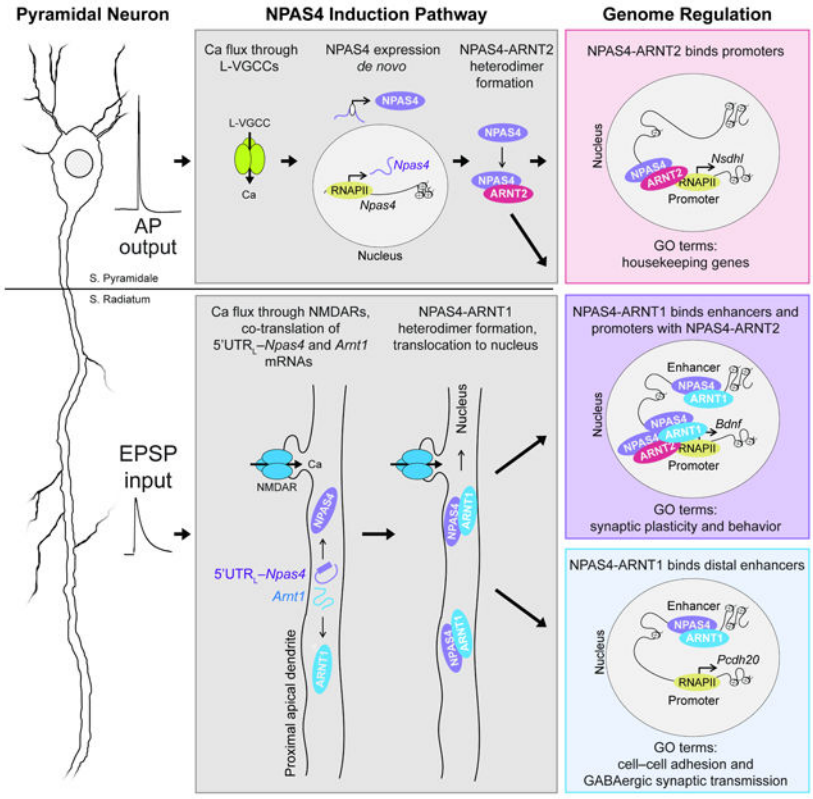

eTOC:

Distinct types of depolarization activity in neurons are transformed by spatially segregated and stimulus-specific transcription factor, NPAS4, heterodimers with different DNA binding patterns.

INTRODUCTION:

Stimulus-dependent gene regulation is a core feature of biological systems and involves the expression of inducible transcription factors (ITFs) that drive subsequent gene regulation tailored to the initial stimulus (Bartel et al., 1989; Cole et al., 1989). From insects to primates, sensory input, behavioral output, and learning trigger ITF expression in the brain (Burmeister et al., 2005; Renier et al., 2016; Sommerlandt et al., 2019). Membrane depolarization is a common trigger for ITF expression in neurons (Bartel et al., 1989; Cochran, 1993; Ghosh et al., 1994; Greenberg and Ziff, 1984; Sheng et al., 1990), and substantial progress has been made in elucidating the mechanisms linking global depolarization to ITF expression (Chen et al., 2019; Joo et al., 2016; Kim et al., 2010; Ma et al., 2014; Madabhushi et al., 2015; Malik et al., 2014; Saha et al., 2011; Sharma et al., 2019; Tyssowski et al., 2018; Wild et al., 2019) Yet, neuronal depolarization is not spatially uniform. Rather, it fluctuates as it propagates from the site of origin. Moreover, depolarization can result from synaptic inputs, in the form of excitatory postsynaptic potentials (EPSPs), or the action potential (AP) output. It is unclear whether expression of a

given ITF can reflect changes in both neuronal input and output and differentially communicate this information to the nucleus.

Among ITFs, NPAS4 is thus far unique; it is induced by depolarization but insensitive to other stimuli (Lin et al., 2008; Ramamoorthi et al., 2011). This specificity allows NPAS4 to selectively communicate a neuron's depolarization's history to the nucleus raising the possibility that NPAS4 may customize gene regulation according to the type of depolarization that triggered its expression. Moreover, NPAS4 functions to regulate synaptic connectivity (Bloodgood et al., 2013; Hartzell et al., 2018; Spiegel et al., 2014; Weng et al., 2018) and *Npas4* knockout (KO) mice exhibit cognitive deficits and seizures (Coutellier et al., 2012). Thus, understanding what types of activity lead to NPAS4 expression will shed light on how depolarization is transformed into changes in synaptic connectivity.

We identify two spatially and molecularly distinct induction mechanisms that trigger NPAS4 expression in response to either APs or EPSPs in CA1 pyramidal neurons (PNs) of the mouse hippocampus. APs trigger *de novo* transcription and translation of NPAS4. EPSPs induce NPAS4 through the translation of dendrite-localized *Npas4* mRNAs that are regulated by a long 5' UTR, a mechanism that to our knowledge is unprecedented for an ITF. These two induction pathways culminate in the formation of stimulus-specific NPAS4 heterodimers. In turn, AP- and EPSP-induced dimers interact with different genomic loci and genes. Through this mechanism, a neuron's AP output and synaptic inputs are transformed into distinct modes of genomic regulation by the same ITF.

RESULTS:

APs and EPSPs engage distinct Ca sources to induce NPAS4 in CA1 PNs.

To investigate the origins of excitatory signals that induce NPAS4, we optimized an acute slice preparation from the mouse hippocampus in which NPAS4 is not induced during cutting and recovery (postnatal day, P21–28; Figure S1A, B). We examined if APs are sufficient to induce NPAS4 in wild-type (WT) mice by evoking antidromic APs in CA1 PNs via extracellular stimulation of the alveus in the presence of the glutamate receptor antagonists NBQX and CPP (Figures 1A and S1C). One hour after stimulation, slices were fixed and stained for NPAS4. Low-frequency stimulation (0.1 Hz for 3.5 min) did not induce NPAS4 and was indistinguishable from unstimulated slices (Figure 1B). However, interposing a single one-second, 100 Hz tetanus led to robust NPAS4 expression in stratum pyramidale (SP) where PN somata reside (Figure 1A, B). This stimulus generated 48 ± 3 APs in nearby PNs (Figure S1C, D). No significant NPAS4 was detected in the neuropil (stratum oriens [SO], stratum radiatum [SR], or stratum lacunosum moleculare [SLM]) indicating NPAS4 was not induced in interneurons (INs). Thus, a one second train of APs is sufficient to induce NPAS4 in the soma of CA1 PNs.

One second of spiking is an exceptionally brief stimulus for inducing an ITF (Pevzner et al., 2012; Tyssowski et al., 2018; Vaccarino et al., 1992), prompting us to ask if the kinetics of NPAS4 expression parallel those reported *in vitro* (Lin et al., 2008). Slices were prepared and stimulated as above but fixed and stained at various times post-stimulation. No significant NPAS4 was detected within 10 min. However, by 15 min NPAS4 was apparent in

SP and increased steadily until 90 min (Figure 1C, D), as previously seen. NPAS4 was not detected in SR at any time point. Bath application of nimodipine (Nim) to antagonize L-type voltage-gated calcium (Ca) channels (L-VGCCs) abolished AP-induced NPAS4 (Figures 1E and S1E), indicating APs signal through L-VGCCs to induce NPAS4.

To determine if synaptic inputs also induce NPAS4, we stimulated afferent axons to evoke EPSPs in specific layers of the neuropil. Voltage-gated sodium and potassium channels were blocked with TTX and 4-aminopyridine (4AP) to prevent APs while facilitating transmission (Buckle and Haas, 1982; Perreault et al., 1989). Local afferents in SO, SR, or SLM were stimulated (one second, 100 Hz; Figure S1F-H), evoking a 4–8 mV EPSP as recorded from a PN near the stimulation electrode (Figure S1G, H). One hour later, slices were fixed and stained for NPAS4 (Figures 1F and S1I). NPAS4 was not detected in somata located in SO, SR, or SLM, suggesting this stimulus does not induce NPAS4 in INs. Intriguingly, EPSPs triggered by SR stimulation, but not SO or SLM, induced NPAS4 (Figures 1G and S1I), indicating that synapses in this layer have a privileged role in eliciting NPAS4 expression.

We determined the time course of NPAS4 expression following stimulation in SR. In contrast to antidromic stimulation, NPAS4 was first detected in dendrites in SR, appearing within three min, peaking at five, and waning thereafter (Figure 1H, I). NPAS4 protein was also detected in PN somata in SP, but lagged behind, being initially detected at 10 min and increasing up to 90 min (Figure 1H, I). The spatial profile of EPSP-induced NPAS4 is conspicuous, as production of NPAS4 in the soma and transport to the dendrites would result in inverted spatiotemporal dynamics from those observed.

Trains of EPSPs produce large NMDAR-mediated Ca signals and can gate L-VGCCs (Magee and Johnston, 1995; Magee, 1995). We determined which Ca source is required for synaptically-induced NPAS4 by stimulating afferents in SR in the presence of NMDA receptor (NMDAR) or L-VGCC antagonists (CPP or Nim; Figure S1J). CPP completely prevented EPSP-induced NPAS4 expression, whereas Nim had no impact (Figure 1J) indicating NMDAR signaling is required. Thus, EPSPs originating in SR and APs induce NPAS4 via distinct Ca sources and result in NPAS4 expression patterns with unique spatiotemporal profiles.

NPAS4 has not been previously observed in dendrites of PNs. To determine if sensory experiences can induce dendritic NPAS4 *in vivo,* we transferred mice (P21–28) from their home cage (HC) briefly into an enriched environment (EE, five min), and then returned them to their HC (Figure 1K). Hippocampi were removed at various times (1–90 min) and stained for NPAS4. In WT mice, NPAS4 was first detected in SR followed by SP (Figure 1L, M), recapitulating our observations in slices. Deletion of *Npas4* in excitatory neurons (*Npas4*$^{f/f}$::*GAD2*^{Cre}) eliminated the experience-dependent NPAS4 induction, whereas *Npas4* KO in INs (Npas4$^{f/f}$::*GAD2*^{Cre}) had no impact (Figure 1N, O), indicating dendritic and somatic NPAS4 protein is produced in PNs. A similar expression profile was observed in CA3 PNs (Figure S2A-D), suggesting that dendritic NPAS4 may be a general feature of PNs (Figure S2E-H). Thus, immediately after novel experiences, NPAS4 is observed in PN dendrites *in vivo,* likely reflecting EPSPs in SR.

Synaptically induced NPAS4 is translated in the dendrites and transported to the nucleus.

The translation of *Npas4* mRNA should take nearly three min (Wu et al., 2016), mirroring EPSP-induced NPAS4 in dendrites and suggesting a mechanism that does not require *de novo* transcription (Darzacq et al., 2007; Okuno et al., 2012). To test this, stimulation was delivered in SR in the presence of the transcription inhibitor actinomycin D (ActD), translational inhibitor anisomycin (ANI), or mTOR inhibitor rapamycin (RAP; Figure S1J). Blocking transcription during synaptic stimulation did not impact the kinetics or magnitude of dendritically localized NPAS4 protein, yet significantly reduced NPAS4 immunoreactivity in SP (Figure 1P, Q). In contrast, inhibiting translation or mTOR signaling prevented EPSP-induced NPAS4 expression (Figure 1R). Evoking antidromic APs failed to induce NPAS4 in the presence of transcription or translation inhibitors (Figures 1S, T and S1E). Together, these data provide evidence that EPSPs in SR lead to NPAS4 translation in dendrites that does not require stimulus-evoked transcription, although transcription boosts somatic NPAS4. In contrast, AP-induced NPAS4 requires transcription.

The spatiotemporal profile of EPSP-induced NPAS4 suggests it is translated in the dendrites and transported to the soma. To visualize the origin and redistribution of newly synthesized NPAS4 over time, we metabolically labeled nascent protein using a puromycin proximity ligation assay (puro-PLA; tom Dieck et al., 2015). Dissociated hippocampal neurons transfected with RFP were silenced (TTX, CPP, and NBQX, 24 hours; 15–16 days *in vitro,* DIV), “pulsed” (three min) with media containing the $GABA_A$ receptor antagonist picrotoxin (PTX) and puromycin (puro), and then “chased” with media (1–90 min; Figure 2A). Stimulus-evoked transcription was inhibited throughout the pulse and chase with ActD. Newly synthesized NPAS4 was detected through amplification of puro and NPAS4 antibodies in close proximity, and was quantified in the nucleus, soma, and dendrites. As the incorporation of puro releases the nascent peptide from the ribosome and the NPAS4 antibody detects the C-terminal portion of the protein, this strategy likely underestimates NPAS4 synthesis.

NPAS4 puncta were first detected in dendrites (Figures 2B, H, and S3A) and subsequently in the soma and nucleus (Figures 2B, H), consistent with the synthesis of NPAS4 in the dendrites and translocation into the nucleus. NPAS4 was not detected in cultures pulsed with TTX, CPP, and NBQX (Figures 2C, I, and S3B), reaffirming that the translation of preexisting *Npas4* mRNAs is activity dependent. When ActD was omitted and puro included in the pulse and chase, significantly more NPAS4 accumulated in the soma and nucleus at 90 min, reflecting the translation of preexisting and *de novo*-synthesized mRNAs (Figures 2D, H and S3C). Furthermore, no NPAS4 was detected when translation was inhibited or when puro was omitted (Figures 2E, F and S3D, E, G), confirming assay specificity. The time course of NPAS4 accumulation in the nucleus suggests an active transport mechanism (Ch'ng et al., 2015; Ch'ng et al., 2012; Wiegert et al., 2007). Disrupting microtubule dynamics with Nocodazole (Noc) during the pulse and chase significantly reduced nuclear accumulation (Figures 2G, I, and S3F), indicating dendritic NPAS4 is actively transported to the nucleus.

To determine if dendritically translated NPAS4 accumulates in the nucleus of PNs in slices, we inhibited translation at different times after stimulation in SR and quantified NPAS4 one

hour later. Application of ANI before or concomitantly with stimulation prevented NPAS4 expression (Figure S3H, I), indicating the translation machinery stalled within minutes. However, when ANI was applied to the slice five min post-stimulation, NPAS4 was detected in SP at levels comparable to ActD but lower than control conditions (Figure S3H, I). As observed *in vitro,* NPAS4 remained in the dendrites and failed to significantly accumulate in the soma when microtubules were destabilized (Figure S3J-M). Thus, NPAS4 translated in dendrites is trafficked via microtubules to the nucleus, where it may contribute to further NPAS4 expression.

Npas4 mRNA is localized to PN dendrites and degraded after translation.

NPAS4 is translated in dendrites, yet its mRNA has not been identified among those enriched in dendrites (Cajigas et al., 2012). We used single-molecule fluorescence *in situ* hybridization (smFISH; Wang et al., 2012) to detect mRNA with high sensitivity, as confirmed by control experiments probing for *CamK2a* and *Grial* (Burgin et al., 1990; Ju et al., 2004; Maghsoodi et al., 2008; Mayford et al., 1996; Figures S3N, O and 2J, K). Probing for the coding sequence (CDS) of *Npas4* in WT mice revealed mRNA localized to soma/nuclei in SP and neuropil in SR but few in SO and SLM (Figures 2J, K). Puncta in SR overlapped with PN dendrites visualized in $Thy1^{GFP}$ mice and by MAP2 staining (Figure S3P). Importantly, *Npas4* was not detected in tissue from *Npas4* KO mice (Figure S3Q, R), and was exclusively localized to *Slc32a1*-positive (alias VGAT) nuclei when *Npas4* was excised from excitatory neurons ($Npas4^{f/f}$::$Emx1^{Cre}$; Figures 2L, N). In contrast, deletion of *Npas4* from INs ($Npas4^{f/f}$::$Gad2^{Cre}$) did not alter *Npas4* localization relative to WT sections (Figure 2M, N). Thus, *Npas4* mRNAs are localized to the apical dendrites of CA1 PNs. Finally, we stained for *Fos* and observed puncta in SP but not in SR (Figure S3S, T), indicating dendritic mRNA is not a general ITF feature.

Restriction of *Npas4* to SR likely underlies the privileged role for these synapses in triggering NPAS4 expression. To test this, we prepared acute slices under RNase-free conditions, stimulated in SR, and performed smFISH at various times post-stimulation. *Npas4* was apparent in SP and SR 10 min after low-frequency stimulation (Figure 2O, P) indicating mRNAs are stable and distributed as *in vivo*. After high-frequency stimulation, the abundance and distribution of mRNAs began to decrease by five min and was significantly depleted by 10–15 min. At the 90-min time point, *Npas4* in the neuropil remained low, whereas mRNA in SP was significantly increased relative to control slices (Figure 2O, P).

The change in abundance of *Npas4* along the somato-dendritic axis could be due to translation-dependent degradation (TDD; Giorgi et al., 2007) of dendritic mRNAs followed by *de novo* transcription of *Npas4*. Alternatively, there could be a stimulus-dependent redistribution of mRNA from the dendrites to soma. To distinguish between these possibilities, we repeated the stimulation in SR with either translation or transcription inhibited. ANI abolished the rapid stimulus-dependent depletion of dendritic mRNA (10–15 min) and the delayed increase in somatic mRNA (90 min, Figure 2P), demonstrating that both changes are coupled to stimulus-dependent translation. In contrast, inhibiting transcription had no impact on the depletion of mRNA in SR but prevented the increase in

somatic mRNAs (Figure 2O, P). These results support a model in which EPSPs in SR lead to the translation then degradation of dendritic *Npas4* mRNAs. Newly translated protein, potentially NPAS4 itself, then signals to the nucleus to promote the further transcription of *Npas4*.

Dendritically localized *Npas4* mRNA encompasses a long 5' UTR.

The two strategies for inducing NPAS4 imply the dendritic mRNAs include cis-regulatory elements that AP-induced *Npas4* mRNAs lack. We examined the *Npas4* gene and noted three predicted variants (Figure 3A) that share CDS exons with the validated transcript but include additional exons that form an extended 5' untranslated region (UTR), opening the possibility that dendritic mRNA may include a long 5' UTR (5' UTR_L). Supporting this, low levels of mRNA that are constitutively expressed, modestly inducible, and map to the predicted 5' UTR_L are present in RNA-seq data sets (Kim et al., 2010). Furthermore, comparison of conservation among 60 vertebrates (Felsenstein and Churchill, 1996) shows that portions of 5' UTR_L first appeared in mammals and are conserved from marsupials to humans (Figure S4).

We designed smFISH probes (Figure 3A) against two regions of 5' UTR_L (5'UTR_1 and 5'UTR_2) that are shared among all three predicted transcripts, two regions of the coding sequence (CDS_1 [used in Figure 2] and CDS_2), and one region of the 3' UTR. None of these probes detected appreciable mRNA in sections from $Npas4^{f/f}$::$Emx1^{Cre}$ mice (Figure 3C), yet all five detected comparable *Npas4* mRNA in the dendrites of CA1 PNs from WT mice in their HC (Figure 3B, C). Probes for 5' UTR_L detected fewer mRNAs in SP (Figure 3C), revealing a relative enrichment for mRNAs localized to SR. This observation is consistent with the *Npas4* gene encoding two pools of mRNA that can be distinguished by 5' UTR_L and subcellular localization. This interpretation, with data from Figures 1P and 2O, predicts that exposure of mice to EE may result in a reduction of *Npas4* in SR detected with any probe set and a concomitant increase in mRNAs in SP exclusively with CDS and 3' UTR probes. Indeed, one hour post-EE, *Npas4* in SR was depleted while mRNAs in SP were significantly induced (Fig. 3D, E), but only as detected with the CDS and 3' UTR probes. Thus, *Npas4* mRNAs encompassing 5' UTR_L are constitutively expressed, localized to the proximal apical dendrites, and their abundance is reduced in response to sensory experience. In contrast, mRNAs lacking 5' UTR_L are restricted to the soma and increase in abundance in response to experience.

How does 5' UTR_L influence the localization and stimulus-dependent translation of mRNA? Neurons were transfected with a control nuclear-localized GFP (GFP_{NLS}), or GFP_{NLS} flanked by the short 5' UTR (5' UTR_S) or 5' UTR_L and the 3' UTR of *Npas4*. Cultures were pulsed with puro (−Stim) or puro plus PTX (+Stim; three min), then chased with media for 15 min. GFP mRNA and nascent protein were quantified using smFISH and puro-PLA assays (Figure 3F-H). GFP mRNA was localized to dendrites in −Stim cells expressing 5'UTR_L-GFP_{NLS}. In response to stimulation mRNA was depleted and nascent GFP protein emerged in dendrites (Figure 3H, I). Neither GFP_{NLS} nor 5'UTR_S-GFP_{NLS} exhibited this behavior (Figure 3F, G, and I), indicating that the long 5' UTR is a key regulator of NPAS4 in dendrites.

Cis-regulatory elements control *Npas4* mRNA translation and localization.

We investigated the utility of conserved regions of the endogenous 5' and 3' UTRs by selectively occluding them via binding of nuclease- and helicase-inactive CRISPR/Cas9 (dCas9, Figure 4A; Nelles et al., 2016; O'Connell et al., 2014). Single guide RNAs (sgRNAs) were designed to recruit dCas9 to two regions of 5' UTR_L, the translational start codon, or a predicted zip code motif in the 3' UTR (Figure 4B; ACACCC…ACAAACCA; Kislauskis et al., 1994; Wu et al., 2015). We confirmed the recruitment of dCas9 to *Npas4* mRNA by transfecting HEK293T cells with plasmids encoding full-length *Npas4* (FL-Npas4), dCas9-GFP, a DNA/RNA oligonucleotide adapter (PAMmer), and a sgRNA. dCas9 and associated RNAs were immunoprecipitated (IP'd) with a GFP antibody, RNA was converted to cDNA, and PCR performed to amplify *Npas4*. sgRNAs complementary to *Npas4* did not impact *Npas4* mRNA levels but were essential for amplification of *Npas4* (Figure S5A). This indicates RNA interference mechanisms were not engaged and that all five recruit dCas9 to *Npas4* mRNA.

We next used dCas9 to manipulate endogenous *Npas4* mRNA. Neurons were co-transfected with dCas9-GFP, a sgRNA and PAMmer, then treated with DMSO (−Stim) or PTX (+Stim). The distribution of *Npas4* mRNA and protein was visualized using smFISH and immunostaining. In – Stim neurons transfected with dCas9 alone or dCas9 plus a control sgRNA (λ2) and PAMmer, mRNAs were detected in the soma and dendrites and NPAS4 protein signal was minimal (Figures 4C, D and S5B, D). Following stimulation, *Npas4* mRNAs were depleted from the dendrites and significantly increased in the nucleus and soma. Concomitantly, NPAS4 protein exhibited significant increases in all compartments (Figures 4C, D and S5B, D).

Next, neurons were transfected with sgRNA targeting the translational start codon (CDS_{ss}; ss: single-stranded), which is common to all *Npas4* transcripts. Under basal conditions, mRNA localization was comparable to control neurons. However, sgRNA-CDS_{ss} prevented the activity-dependent reduction of dendritic mRNA and synthesis of protein (Figures 4E and S5D), reflecting occlusion of the translation start site and providing additional evidence for TDD. Next dCas9 was targeted to two conserved regions of 5' UTR_L (5'UTR_1 and 5'UTR_2). In cells expressing sgRNA-5'UTR_1, mRNA and protein distribution were indistinguishable from control transfected neurons, suggesting this region is not involved in controlling mRNA localization, stability, or stimulus-dependent translation (Figure S5B-D). In contrast, recruitment of dCas9 with sgRNA-5'UTR_2 prevented stimulus-dependent mRNA depletion and protein synthesis in the dendrites (Figure 4F) without impacting mRNA and protein in the soma (Figure 4F), underscoring the segregated signaling pathways. Finally, recruitment of dCas9 to the 3' UTR significantly reduced dendritic mRNA puncta in −Stim cells, and consequently dendritic protein synthesis (Figure 4G). Together, these data indicate that nucleotides occluded by sgRNA-5'UTR_2 are essential for the stimulus-dependent translation of dendritic *Npas4* mRNA, and the 3'UTR plays a critical role in mRNA trafficking into dendrites.

We next utilized catalytically active Cas9 to disrupt DNA sequences occluded by sgRNA-5'UTR_2 (Figure 4H). We screened the 5' UTR_2 region for putative structural (RNAstructure; Reuter and Mathews, 2010) and functional motifs (regRNA2.0; Chang et al.,

2013), identifying two adjacent modules with possible roles in regulating translation: a sequence evocative of an internal ribosomal entry site (IRES; Le and Maizel, 1997), followed by a short upstream open reading frame (uORF; Figure 4I). These elements could work to assemble and stall the ribosome on the mRNA until stimulus presentation (Hinnebusch et al., 2016; Kieft, 2008). To test this, neurons were co-transfected with RFP and a bi-cistronic construct encoding Cas9 and a sgRNA that was either non-targeting (scramble), or targeted the translational start site (CDS_{ds}; ds: double-stranded), putative IRES ($5'UTR_{2a}$), or uORF ($5'UTR_{2b}$; Figure 4I). sgRNAs were validated using a T7 nuclease assay (Guschin et al., 2010; Rubio et al., 2016) and all edited FL-Npas4 (Figure S5E).

In neurons transfected with Cas9 and sgRNA-scramble, mRNA and protein distribution in control- and PTX-treated cultures were comparable to dCas9-transfected cells (Figures 4J, K and S5F) indicating Cas9 did not disrupt *Npas4* transcription or translation. Importantly, mRNA localization in sgRNA-CDS_{ds} cells was also similar to controls in ±Stim conditions (Figure 4L), indicating that disruption of the translational start site, downstream of transcription initiation, did not impact mRNA. NPAS4 protein, however, was not detected, reflecting disrupted translation or the synthesis of a null protein (Figure 4L). Targeting Cas9 to the putative IRES (sgRNA-$5'UTR_{2a}$) did not impact dendritic mRNA localization under basal conditions (Figure 4M). Upon stimulation however, dendritic mRNAs persisted and dendritic protein was not detected, despite increased somatic mRNA and protein (Figure 4M). These data suggest Cas9 editing of the putative IRES prevented activity-dependent translation and degradation. Finally, targeting Cas9 to the uORF (sgRNA-$5'UTR_{2b}$) reduced mRNA in the dendrites, but led to protein in the nucleus in −Stim conditions (Figure 4N). Activity failed to change dendritic mRNA and protein abundance while somatic and nuclear protein significantly increased (Figure 4N). Thus, disruption of the uORF resulted in constitutive NPAS4 expression, most parsimoniously due to a loss of translational repression. These results implicate two discrete cis-regulatory elements in 5' UTR_L that control translation in dendrites: an IRES-like structure required for translation and an adjacent uORF that prevents translation in the absence of activity.

We next assessed whether Cas9 editing of *Npas4* could impact EE-driven changes in mRNA localization and abundance *in vivo*. CA1 of mice (P14–16) constitutively expressing Cas9 (*H11*$^{Cas9\text{-}FLAG}$; Chiou et al., 2015) were infected with adeno-associated virus (AAV) encoding a sgRNA and nuclear-localized GFP-KASH ($AAV_{2.1}$_U6-sgRNA_hSyn-GFP_{nuc}; Figure 4O). At P21-23, smFISH for *Npas4* (CDS_1) and GFP was performed on sections from mice obtained from HC or EE (Figure S5G). In HC mice, *Npas4* mRNA was abundant in SR when CA1 was infected with AAV-sgRNA-scramble, sgRNA-CDS_{ds}, or sgRNA-$5'UTR_{2a}$, but was depleted when infected with sgRNA-$5'UTR_{2b}$ (Figure 4P), in agreement with the role of the uORF *in vitro* (Figure 4K, L). After EE, mRNAs were depleted from SR with the exception of CA1 infected with sgRNA-$5'UTR_{2a}$ (Figure 4Q), indicating that disruption of the putative IRES prevents translation of dendritic *Npas4* mRNA *in vivo*. EE-induced *Npas4* in SP regardless of the sgRNA expressed, indicating activity-dependent *de novo* transcription of *Npas4* was not disrupted (Figure 4Q). Notably, the EE-induced somatic mRNA was attenuated in tissue infected with AAV-sgRNA-CDS_{ds} (Figure 4Q) suggesting that disruption of NPAS4 translation diminishes *de novo*

transcription of *Npas4*. In sum, these data demonstrate a synergistic requirement for two cis-regulatory elements in 5' UTR_L for regulation of stimulus-driven translation of dendritic *Npas4 in vivo*.

NPAS4 forms stimulus-specific heterodimers.

NPAS4 is expressed in response to APs or EPSPs, yet it is unclear how this information is preserved in the nucleus. NPAS4 must heterodimerize with a member of the '*Arnt* subfamily' of transcription factors (TFs) to bind DNA (Bersten et al., 2013). ARNT1 (alias ARNT), and ARNT2 are known to associate with NPAS4 and, together with ARNTL1 (alias BMAL1), are expressed in the hippocampus (Lipton et al., 2015; Ooe et al., 2009; West et al., 2013). We hypothesized that AP- and EPSP-induced NPAS4 may form distinct heterodimers, thereby succinctly communicating changes in the neuron's output and inputs to the genome.

Acute slices were stimulated in the alveus or SR, CA1 microdissected, and lysates probed by Western blot (WB) for NPAS4 and ARNT subfamily members (see Figure S6A). ARNT1, ARNT2, and ARNTL1 were constitutively expressed in CA1 and NPAS4 was induced in response to APs and EPSPs (Figure 5A, B, E, and F). Next, NPAS4 was IP'd and blots probed with antibodies against ARNT subfamily members. AP-induced NPAS4 associated with ARNT2 at 60 min post-stimulation, at the exclusion of ARNT1 and ARNTL1 (Figure 5C, D). In stark contrast, EPSP-induced NPAS4 exclusively associated with ARNT1 both at five min, when the NPAS4 is in the dendrites, and 60 min post-stimulation, after NPAS4 has translocated to the nucleus (Figure 5G, H). Thus, NPAS4 forms distinct heterodimers in response to different excitatory stimuli, revealing a mechanism through which the genome may disambiguate depolarization due to APs or EPSPs.

The rapid association of NPAS4 with ARNT1 implies that, in spite of its constitutive presence in the nucleus and soma, ARNT1 may transiently localize to dendrites. smFISH for *Arntl* mRNA revealed a distribution that paralleled *Npas4* (Figure S6B, C) while *Arnt2* did not (Figure S6D, E), suggesting *Npas4* and *Arnt1* may be translated concurrently. To test this, acute slices were stimulated in SR and stained for NPAS4, ARNT1 or ARNT2. In response to low frequency stimulation, none of the three were detected in dendrites spanning SR. High-frequency stimulation in SR, however, led to rapid expression of ARNT1, but not ARNT2, in SR that colocalized with NPAS4, accumulated in SP over time, and required NMDAR activation (Figure S6F-H). Thus, NPAS4 and ARNT1 are translated in the dendrites in response to EPSPs, underlying stimulus-specific dimerization.

Sensory experiences trigger rapid dendritic, followed by somatic, expression of NPAS4. The dendritic protein can be attributed to EPSPs, yet it is unclear if the somatic protein reflects EPSP- or AP-induced NPAS4. We disambiguated these possibilities by assessing NPAS4 heterodimer formation in response to EE. Mice were transferred from their HC to an EE for five min, returned to their HC, and then hippocampi dissected and lysed for WB analysis (Figure 5I). ARNT1 and ARNT2 were expressed constitutively and equivalently. NPAS4 was significantly induced at five min and steadily increased to 90 min (Figure 5I, J). At early time points (5–15 min), NPAS4 IP'd exclusively with ARNT1, confirming dendritically synthesized NPAS4 dimerizes with ARNT1 *in vivo* (Figure 5K, L). By 90 min post-EE,

NPAS4 associated with ARNT1 and ARNT2 (Figure 5K, L), demonstrating that EE drives EPSP- and AP-induced NPAS4 signaling pathways *in vivo*.

Next, we tested if the cis-regulatory elements in 5' UTR_L are necessary for the specificity of heterodimer formation *in vivo*. AAVs encoding sgRNAs were injected into CA1 of *H11*$^{Cas9\text{-}FLAG}$ mice (P14–16). Two weeks later, mice were maintained in HC or exposed to EE (five min) then returned to HC (five or 90 min; Figure 5M). Neurons infected with sgRNA-scramble exhibited the expected experience-dependent NPAS4 profile, interacting with ARNT1 five min post-EE and both ARNT1 and ARNT2 at 90 min (Figure 5N-Q). NPAS4 was not detected when the translational start site was edited (sgRNA-CDS_{ds}; Figure 5N, O). Disruption of the putative IRES (sgRNA-5'UTR_{2a}) prevented the rapid expression of NPAS4, consistent with a failure to translate dendritic mRNAs, but at 90 min post-EE NPAS4 was expressed and precipitated with both ARNT1 and ARNT2 (Figure 5N-Q). This suggests dendritic NPAS4-ARNT1 dimerization may indirectly facilitate the specificity of AP-induced heterodimers, perhaps by reducing the availability of ARNT1. Lastly, targeting Cas9 to the uORF (sgRNA-5'UTR_{2b}) significantly increased basal NPAS4 expression with only a modest increase at 90 min and both heterodimers were detected in all samples (Figure 5N-Q), revealing a collapse of the stimulus-specific heterodimer formation. Thus, the spatial and temporal control of dendritic *Npas4* translation via cis-regulatory elements in the 5' UTR enables the unambiguous formation of EPSP- and AP-specific NPAS4 heterodimers *in vivo*.

NPAS4 heterodimers bind different regions of the genome.

Do the two NPAS4 heterodimers differentially interact with the genome? We evaluated genomewide DNA binding of NPAS4, ARNT1 and ARNT2 and gene expression in silent ("−"; TTX, CPP, and NBQX; 24 hours) or stimulated ("+"; PTX; 2 hours) neurons (DIV 28). NPAS4-ARNT1 and NPAS4-ARNT2 heterodimers were detected in stimulated but not silenced cells (Figure S7A-D). High-quality ChIP-seq data were generated from two biological replicates for the three TFs, as well as RNA polymerase II (RNAPII) and histone H3 lysine 27 acetylation (H3K27ac) to identify highly transcribed genes and active enhancers/promoters (Figure S7E; Creyghton et al., 2010; Rada-Iglesias et al., 2011; Ramirez et al., 2014).

Sequencing of NPAS4-bound DNA from stimulated neurons revealed ~32,000 peaks (FDR=0.001) while ~100 were detected in silenced cells (Figure 6A and Table S2). ARNT1 and ARNT2 binding were strikingly different: both exhibited tens of thousands more peaks than NPAS4 (ARNT1: ~120,000 peaks, Table S3; ARNT2: ~60,000 peaks, Table S4), likely reflecting binding of homodimers and heterodimers formed with other bHLH-PAS TFs (Kewley et al., 2004; Sharma et al., 2019; Swanson et al., 1995). Upon stimulation, ARNT2 binding generally increased while changes in ARNT1 peaks were highly variable (Figure 6B, C), alluding to different functions for the two TFs and non-uniform responses to activity.

The sites bound by NPAS4 demonstrated activity-dependent increases in RNAPII and H3K27ac (Figure 6D, E and Table S5), implying these are sites of active gene regulation. NPAS4 peaks were distributed throughout the genome, with 6% at a promoter or transcription start site (TSS), 3% at CpG-rich regions, 36% at intragenic locations, and 55%

at intergenic locations (Figure 6F), reflecting an overall preference for putative enhancers over promoters (Kim et al., 2010). Nearly all of the NPAS4 peaks co-localized with ARNT1 and/or ARNT2, but with a clear asymmetry: 43% of NPAS4 peaks coincided with ARNT1, 3% with ARNT2, and 49% with both (Figure S7F). This suggests NPAS4-ARNT2 rarely functions independently of NPAS4-ARNT1, whereas NPAS4-ARNT1 may function independently of, or synergistically with NPAS4-ARNT2.

To elucidate the interactions between AP- and EPSP-induced NPAS4 with DNA, we assessed global patterns of NPAS4, ARNT1, and ARNT2 binding. NPAS4 peaks in +Stim cells were sorted based on the $\log_2$ ratio of binding by ARNT1 and ARNT2 and separated into quartiles (Q1–4; Figure 6G and Table S6). Sites in Q1 exhibited the most prominent H3K27ac and RNAPII signal, substantial pre-binding of ARNT2, and stimulus-triggered ARNT2 binding significantly exceeded ARNT1 (Figures 6G and S7G). In addition, Q1 was dramatically enriched for TSS/promoters and CpG-rich regions, accounting for the bulk of these genomic elements bound by NPAS4. Thus, NPAS4-ARNT2 heterodimers correspond with high levels of transcriptional activity and preferentially bind promoters/TSSs.

In the remaining quartiles, ARNT1 predominated significantly over ARNT2 (Figure 6G and S7G). These sites were enriched for intra- and intergenic loci, depleted of promoters/TSSs, and exhibited increasing activity-dependent H3K27ac signal from Q2 to Q4. Collectively, this suggests that EPSP-induced NPAS4-ARNT1 heterodimers bind enhancers. Exemplifying this, the promoter of the *Nr4a3* gene was bound by NPAS4 with predominant ARNT2, while distal NPAS4 peaks at putative enhancers were enriched for ARNT1 (Figure 6H).

To further understand how NPAS4 heterodimers differentiate among genomic sites, we analyzed the sequences underlying NPAS4 peaks (±175 nucleotides) for TF consensus motifs (HOMER *de novo* motif analysis, Heinz et al., 2010). In Q1, an E-box core recognized by ARNT-family bHLH-PAS TFs was the top-ranked motif, but was not among the top-five motifs in Q3 and Q4 (Figure S7H-L; Kewley et al., 2004; Ooe et al., 2004). The latter quartiles shared enrichment for motifs recognized by EGR2, MEF2, and NeuroD1 families of TFs, and broad overlap with AP-1–like bZIP motifs (Malik et al., 2014; Figure S7J-K). These results were verified by hierarchical clustering of motif enrichment (Figure 6I) and logistic regression of motif presence within peaks (Figure S7M). Together, these analyses reveal that AP-induced NPAS4 likely binds DNA via a canonical bHLH-PAS motif, whereas EPSP-induced NPAS4 binding at enhancers does not. Moreover, the diversity of binding motifs present at NPAS4-ARNT1-bound sites suggests the versatile engagement of enhancers by many activity-dependent TFs.

The divergent patterns of co-binding by ARNT1 and ARNT2 with NPAS4 allude to distinct contributions from each heterodimer toward gene regulation. We assessed activity-dependent changes in gene expression by total RNA-sequencing. Indeed, NPAS4 bound at or near all genes that exhibited two-fold or greater changes in expression, with many genes associated with multiple peaks (Figure 7A and Table S6). We hypothesized that NPAS4-bound genes with greater ARNT2 co-binding may exhibit the largest activity-dependent increases in expression, as NPAS4-ARNT2 favors promoters and has been reported to relieve

transcriptional suppression (Sharma et al., 2019). However, the ratio of ARNT1 to ARNT2 at NPAS4 peaks nearest activity-induced gene's TSS did not co-vary with gene induction, (Figure 7B), indicating that highly induced genes are not associated with binding of a specific NPAS4 dimer.

The preference of a given NPAS4 heterodimer for promoters or enhancers implied that a heterodimer might engage distinct sites along activity-regulated gene loci. Quantifying the relative binding by ARNT1 and ARNT2 at NPAS4 peaks against their distance from the TSS of the nearest upregulated gene confirmed that ARNT2 was enriched relative to ARNT1 only within 1 kb of the TSS, whereas co-binding by ARNT1 predominated significantly at distal sites (Figure 7C-E). Gene ontology (GO) analysis (Metascape; Zhou et al., 2019) of activity-upregulated genes with NPAS4 bound at increasing distance from the TSS indicated that genes with the most proximal NPAS4 peaks are enriched for generalized housekeeping functions (Figure 7F, G). As genes with more distal sites were included the significant GO terms broadened to include behavior and synaptic plasticity (Figure 7F, H). Intriguingly, functional terms emerged from genes bound exclusively at the most distal sites including cell-cell adhesion molecules and GABAergic synaptic transmission (Figure 7F, I). These findings portend an underlying logic to the organization of activity-dependent gene regulation where AP- and EPSP-induced NPAS4 heterodimers cooperate to regulate the promoters of housekeeping genes whereas EPSP-induced NPAS4 engages enhancers to regulate synapses and plasticity.

DISCUSSION

We have identified two spatially segregated and molecularly distinct induction mechanisms that lead to NPAS4 expression in response to increases in AP output or synaptic inputs. The specificity of EPSP-induced NPAS4 stems from the translation of mRNAs localized to SR. These mRNAs are distinguishable via an evolutionarily recent, exceptionally long 5' UTR (Mignone et al., 2002) containing cis-regulatory elements that enable stimulus-dependent translation. Since TFs are enriched for longer-than-average 5' UTRs (Kozak, 1987), additional TFs may exploit 5' UTRs to similar effect. We have also identified a zipcode motif in the 3' UTR required for dendritic trafficking (Kislauskis et al., 1994; Wu et al., 2015). The 3' UTR appears to be common among *Npas4* transcript variants, yet only those with the long 5' UTR are in dendrites. Perhaps mRNAs with the short 5' UTR are translated immediately, out-competing the trafficking machinery. Alternatively, additional cis-elements in the long 5' UTR or unidentified distinctions among 3' UTRs of *Npas4* may be key (Tushev et al., 2018).

Dendritically localized *Npas4* mRNAs are substrates of TDD, suggesting the presence of an excitation-transcription coupling "refractory period" lasting until dendritic mRNAs are replenished (Kosik, 2016). Furthermore, during extended depolarization, nascent ribosome-associated NPAS4 peptides can be rapidly degraded by membrane anchored proteasome complexes (Ramachandran et al., 2018), indicating that neurons utilize multiple mechanisms to restrict the duration and level of NPAS4 expression.

APs and EPSPs induce NPAS4 that forms stimulus-specific heterodimers. We found that *Arnt1* mRNA is localized to the dendrites and translated in response to synaptic activity, enabling EPSP-induced heterodimer formation. It is less clear what mechanisms constrain AP-induce NPAS4-ARNT2 heterodimer formation. One possibility is the involvement of ARNT2-selective co-factors that facilitate dimer assembly or function (Sullivan et al., 2016). Many TF families function as heterodimers, including FOS-JUN and CRTC1-CREB, raising the prospect that analogous mechanisms are utilized to convey spatiotemporal aspects of multiple signaling modalities to the nucleus.

Stimulus-specific NPAS4 heterodimers exhibit divergent patterns of DNA binding, allowing gene regulation to be tailored to fluctuations in the inputs or output of the neuron. AP-induced NPAS4-ARNT2 heterodimers bind sites enriched for the canonical bHLH-PAS–binding motif (Kewley et al., 2004), whereas EPSP-induced NPAS4-ARNT1 heterodimers do not. This suggests that NPAS4-ARNT1 may be a component of a larger DNA-binding complex with a site selectivity that supersedes that inherent to the heterodimer. The C-termini of ARNT1 and ARNT2 are highly divergent, possibly supporting protein-protein interactions that are the true dictators of chromatin binding.

Finally, activity-regulated genes with NPAS4 bound at the TSS or promoter exhibit binding by both ARNT1 and ARNT2, whereas distal NPAS4 sites are overwhelmingly favored by ARNT1. These distance-dependent differences in binding correspond to provocative shifts in target gene function – from housekeeping genes to more brain, synapse, and connectivity-specific genes. These distinctions will likely become more prominent and informative as activity patterns that better mimic endogenous activity are used to study gene regulation. In the particular case of NPAS4, APs and EPSPs result in the production of two heterodimers. Yet the supply chain for producing NPAS4-ARNT1 is finite and takes time to replenish while NPAS4-ARNT2 can be produced in an ongoing manner and in large quantities. Artificial manipulations of membrane potential will undoubtedly skew the ratio of these two heterodimers, obscuring our ability to decipher activity-dependent gene regulation. Improved methods for studying protein-DNA interactions *in vivo* and at the single cell level are needed.

Together, we have identified layers of regulation that underlie NPAS4 expression and enable the genome to decode and respond to precise types of depolarizing signals. This study opens the intriguing possibility that mRNAs for additional TFs may be localized to other dendritic regions. Domain-delimited and stimulus-dependent local translation of TFs may serve as labeled lines of communication allowing the nucleus to survey the activity of a neuron with extraordinary spatial and temporal precision.

STAR Methods

Lead Contact and Materials Availability

Further information and requests for resources and reagents should be directed to and will be fulfilled by the Lead Contact, Brenda L. Bloodgood (blbloodgood@ucsd.edu).

Materials Availability—Plasmids generated in this study have been deposited to Addgene or are available upon request from the Lead Contact.

Experimental Model and Subject Details

See Key Resources Table for detailed list of mouse models and cell lines used in this study.

Mouse Husbandry and Surgery—All animal procedures and protocols were performed in accordance with the University of California San Diego Institutional Animal Care and Use Committee. The following mouse lines were used: wildtype (WT; C57BL/6J), *Npas4*$^{-/-}$ and *Npas4*$^{f/f}$ (Lin et al., 2008), *Emx1*^{Cre} (Gorski et al., 2002), *Gad2*^{Cre} (Taniguchi et al., 2011), Thy1^{GFP} (Feng et al., 2000), and H11$^{Cas9\text{-}FLAG}$ (Chiou et al., 2015). Mouse sex was not explicitly determined; experiments utilized both female and male mice, and data from both sexes was pooled.

All electrophysiology, immunohistochemistry, and fluorescence *in situ* hybridization experiments were performed on mice between postnatal days 21–28 (P21–28) that had been housed in standard conditions (i.e. home cage). For experiments involving exploration of an enriched environment, mice (dam with litter) were transferred from their home cage to a larger open field arena (approximately 53.34 cm × 46.99 cm) under uniform illumination that contained wooden blocks, plastic toys, and several other objects that the animals could investigate but not hide in. Mice were allowed to explore for 5 min, and then returned to their home cage for variable durations of time before tissue was removed for experiments. The dam was not used for experiments. Home cage control mice were handled and placed back in their home cage for 5 min before tissue harvesting. Individual mice from a minimum of three separate litters were used for each experiment.

Stereotaxic viral injections were performed on P14–16 mice weighing 5–9 g. Animals were administered Flunixin (2.5 mg/kg) subcutaneously pre-operatively and post-operatively every 12 h for 72 h. Animals were deeply anesthetized with isoflurane for the duration of the surgery (initially 3–4% in O_2, then maintained at 2%) and body temperature was maintained at 37°C. The fur covering the scalp was shaved and the scalp was cleaned with three iterations of betadine and 70% ethanol before an incision was made to expose the skull. A small burr hole was drilled through the skull over the CA1 region of the hippocampus bilaterally (from Bregma, in mm: medial/lateral: 3.0 (for 5–7 g mice) or 3.1 (7–9 g mice); anterior/posterior: −2.4; dorsal/ventral: 2.8 and 2.9 (5–7 g mice) or 2.85 and 2.95 (7–9 g mice) below the dura) and virus was injected (350 nL at each dorsal/ventral site for a total of 700 nL; 150 nL min^{-1}). Each adeno-associated virus (AAV) was injected as stock titer and not diluted. Three min post-injection, the needle was retracted, the scalp sutured and the mouse was recovered at 37°C before being returned to its home cage.

Cell culture

Primary Neuronal Cultures: Hippocampi from P0 Sprague–Dawley rats were prepared as previously described (Djakovic et al., 2012), and plated at a density of 130 cells per mm^2. Sex was not determined and neurons from male and female pups were pooled. Neurons were grown in maintenance media consisting of Neurobasal media (ThermoFisher Scientific

Cat#21103049) supplemented with Glutamax (ThermoFisher Scientific Cat#35050061), Pen/Strep (ThermoFisher Scientific Cat#10378016), and B27 supplement (ThermoFisher Scientific Cat#17504044).

For smFISH and immunostaining experiments, neurons were transfected with Lipofectamine 2000 (ThermoFisher Scientific Cat#11668019) at 8–10 days *in vitro* (DIV), according to the manufacturer's recommendations, and used for experiments at 14–16 DIV.

For ChIP-seq and RNA-seq experiments, neurons were grown in maintenance media until 28 DIV. To augment neuronal activity, cells were incubated in 50 μM picrotoxin (PTX) reconstituted in dimethyl sulfoxide (DMSO) and diluted in maintenance media for the indicated times (smFISH, puro-PLA, and immunostaining experiments) or 2 h (ChIP-seq and RNA-seq experiments). Cells treated with equivalent volume of DMSO were used as controls unless otherwise indicated. To silence neuronal activity for ChIP-seq and RNA-seq experiments, cells were incubated in (μM): 1 tetrodotoxin citrate (TTX), 10 (R)-CPP (CPP), and 10 NBQX disodium salt (NBQX) reconstituted in water and diluted in maintenance media for 24 h prior to harvesting on day of experiment. Neurons were continuously maintained at 37°C and 5% CO_2 until harvesting or fixation.

Heterologous Cultures: Human embryonic kidney 293 T-variant (HEK293T; ATCC CRL-3216) cells were maintained in Dulbecco's Modified eagle medium (DMEM; ThermoFisher Scientific Cat#10569044) supplemented with 10% fetal bovine serum (ThermoFisher Scientific Cat#16000044), and Pen/Strep. Cells were continuously maintained at 37°C and 5% CO_2. HEK293T are thought to be derived from an epithelial or neuronal lineage from female embryonic human kidney tissue. Our cell line was not authenticated. Cells were transfected using 1% Polyethylenimine Max (Polysciences Inc. Cat#24765-1), according to the manufacturer's recommendations.

Method Details

See Key Resources Table for detailed list of antibodies, select pharmacological chemicals, kits, and other critical reagents used in this study.

Acute Slice Preparation—Transverse hippocampal slices were prepared from mice (P21–P28). Animals were anesthetized by inhalation of isoflurane, and killed by decapitation. The cerebral hemispheres were quickly removed and placed into ice-cold choline-based artificial cerebrospinal fluid (choline-ACSF) consisting of (in mM): 110 choline-Cl, 25 $NaHCO_3$, 1.25 Na_2HPO4, 2.5 KCl, 7 $MgCl_2$, 25 glucose, 0.5 $CaCl_2$, 11.6 ascorbic acid, 3.1 pyruvic acid and equilibrated with 95% O_2 / 5% CO_2. Blocking cuts were made and tissue transferred to a slicing chamber containing choline-ACSF. Slices (300 μm) were cut with a LeicaVT1000 s vibratome (Leica Instruments) and transferred to a holding chamber containing ACSF consisting of (in mM): 127 NaCl, 25 $NaHCO_3$, 1.25 Na_2HPO_4, 2.5 KCl, 2 $CaCl_2$, 1 $MgCl_2$, 25 glucose, saturated with 95% O_2 / 5% CO_2, and supplemented with 250 μM kynurenic acid (KYN) and 0.2 μM TTX. Slices were incubated at 31°C for 30 min and then maintained at room temperature (RT) for the duration of experiment up to 6 h.

Electrophysiology—Whole-cell current clamp recordings were obtained from CA1 pyramidal neurons visualized with infrared, differential interference contrast (IR-DIC) microscopy. Slices were perfused (2–4mL per min) in ACSF, as described above, and all recordings were performed at RT.

Neurons that required ≥ −50 pA of current (I_h) to hold at a membrane potential of −70 mV were discarded. Patch pipettes (open pipette resistance 3–6 MΩ) were filled with an internal solution consisting of (in mM): 147 K-gluconate, 20 KCl, 10 Na_2-phosphocreatine, 10 HEPES, 2 Na-ATP, 0.3 Na-GTP, 5 $MgCl_2$, 0.2 EGTA, and 3% biocytin (Sigma Aldrich B4261). Osmolarity and pH were adjusted to 290–300 mOsm and 7.3 with double distilled water and KOH, respectively. Series resistance (R_s < 25 MΩ) was uncompensated, and cells were discarded if their R_s changed ≥ 20% over the duration of recording.

APs or EPSPs were isolated with bath application of (in μM): 0.2 TTX and 100 4-aminopyridine (4AP), or 10 CPP and 10 NBQX, respectively. Extracellular stimulation of local axons within specific lamina of the hippocampus was delivered by current injection through a theta glass stimulating electrode that was placed in the center of the relevant layer (along the somatodendritic axis of the CA1 neuron) parallel to the patched cell. In experiments evaluating AP-induced NPAS4 (i.e. CPP + NBQX), stimulus strength was adjusted until an antidromic AP was reliably evoked in the patched cell, typically 100–200 μA. In experiments evaluating EPSP-induced NPAS4 (i.e. TTX + 4AP), stimulus strength was set to evoke a 4–8 mV EPSP (typically 50–75 μA). Baseline recordings were obtained by delivery of a single stimulus pulse (0.2 ms pulse width) at 0.1 Hz for 3.5 min. Subsequently, a 1 sec train of stimuli at 100 Hz or a single pulse where 0.1 Hz is indicated was delivered followed by resumption of stimulation at 0.1 Hz for the indicated time points, up to 15 min. The patch pipette was then retracted slowly and diagonally, under visual control in voltage-clamp, to facilitate resealing of the cell's membrane and subsequent processing for biocytin reconstructions. Additional pharmacology included bath application or wash-in of the following (in μM): 20 Nimodipine (Nim), 25 anisomycin (ANI), 25 actinomycin D (ActD), 1 rapamycin (RAP), 0.2 nocodazole (Noc), and 5 colchicine (Colch). All were reconstituted in ddH_2O or DMSO and dissolved in ACSF (See Key Resources table).

Biocytin-labeling and Immunohistochemistry (IHC)—CA1 pyramidal neurons were filled through the patch pipette with an internal solution, described above, containing 3% biocytin and cellular volume was labeled using a diaminobenzene (DAB) reaction, as previously described with modifications (Marx et al., 2012). Briefly, whole-cell patch clamp recordings were obtained from neurons and held for a minimum of 15 min. The patch pipette was slowly detached, and the slice placed immediately in 16% paraformaldehyde (PFA; Electron Microscopy Sciences Cat#15710) diluted to 4% final concentration in phosphate buffered saline (PBS) at 4°C for 2 h on a shaking p latform. All the following steps were carried out at 4°C on a rotating platform and all washes were 10 min, unless otherwise noted. Slices were washed 6x in 100 mM Phosphate Buffer (PB; consisting of NaH_2PO_{4-} and $NaPO_{4-}$, pH 7.4), incubated for 20 min in PB + 3% H_2O_2, washed 4x in PB, then incubated overnight in a permeabilization buffer (3% Triton X-100, 2% normal goat serum (NGS; Sigma Aldrich Cat#S26) in PB). The next day, slices were washed 1x in PB,

incubated for 2 h in a ‘pre-incubation’ buffer (0.5% Triton X-100, 0.5% NGS in PB), and then incubated in a biotinylation buffer (pre-incubation buffer + ABC solutions (See Key Resources Table; 1% of “Reagent A” Avidin + 1% “Reagent B” biotinylated horseradish peroxidase) for 2 h. Slices were then washed 3x in PB, 2x in Tris Buffer (TB; 50 mM Tris base, pH 7.4), incubated for 10 min at RT in DAB solution 1 (1% Imidazole, 1 tablet / 2 mL DAB (Sigma Aldrich Cat#D5905), in TB), and then incubated in DAB solution 2 (1% Imidazole, 1% Ammonium nickel sulfate hydrate $(NH_4)_2Ni(SO_4)_2$, 1 tablet / 2 mL DAB, 3% H_2O_2, in TB) for 2–10 min at RT, or until the slices turned visibly dark purple. Slices were immediately washed in PB for 1 min, followed by 2x washes in PB.

Following biocytin-labeling, slices were processed for immunohistochemistry (IHC). After 2x washes in PB, slices were incubated in primary antibody solution (0.25% Triton X-100, 2% NGS, in PB plus diluted antibodies) for 48 h at 4°C on a rotating platform. Slices were then washed 3x in PB, and incubated for 24 h in secondary antibody solution (0.25% Triton X-100, 2% NGS, in PB plus diluted secondary dye-conjugated antibodies). Slices were then washed 3x in PB, the biocytin fill was examined through a light microscope to determine the slice mounting orientation, slices were mounted biocytin label side-up on a Superfrost Plus slide (Fischer Scientific Cat#22-037-246), embedded in Fluoromount G mounting media (Electron Microscopy Sciences Cat#17984-25), and cover slipped.

Tissue section IHC—Mice were anesthetized and killed by decapitation as described above, hippocampi dissected, and incubated in 4% PFA / PBS at 4°C for 2 h with g entle agitation. Post-fixation, hippocampi were incubated in 30% sucrose / PBS at 4°C for 48 h, and embedded in Optimal Cutting Temperature compound (OCT; Tissue Tek Cat#4583) at −80°C. Fresh-fixed hippocampi were cryosectioned in the coronal plane at 20 μm, collected on Superfrost Plus glass slides and subsequently stored at −20°C until IHC processing. First, slides were incubated in 0.25% Triton X-100, 2% NGS, in PBS overnight at 4°C with gentle agitation. The next day, slides were incubated in the same solution plus diluted primary antibodies at 4°C for 48 h with gentle agitation. Slides were then washed 3x in PBS, incubated at 4°C for 24 h with gentle agitation in the above solution plus diluted secondary antibodies, washed 3x in PBS, embedded in Fluoromount G mounting media, and cover slipped.

Puromycin-Proximity Ligation Assay (puro-PLA)—The puro-PLA pulse-chase assay was performed as previously described (tom Dieck et al., 2015) with modifications. Briefly, dissociated rat hippocampal neurons were transfected with the indicated cDNA constructs at DIV 8, and seven days later were either activity silenced for 24 h in media containing (in μM): 0.5 TTX, 10 CPP, and 10 NBQX or treated with media containing DMSO. The next day, media was removed, and cells were pulsed with media containing 1 μM puromycin, 50 μM PTX, and ± 25 μM ActD for 3 min, then removed and replaced with media containing ± ActD, and incubated (chased) for various time points. Negative control cells were pulsed for 3 min with media omitting puromycin, or media containing puromycin plus the same activity silencing drugs, or plus PTX, ActD, and 25 μM ANI. Cells pulsed with PTX but without ActD included puromycin in the 90 min chase step. Treatment with Noc was conducted for the duration of pulse and 90 min chase steps. Following pulse-chase steps

cells were washed twice in pre-warmed (37°C) PBS supplemented with 1 mM MgC l_2 plus 0.1 mM $CaCl_2$ (PBS-CM), fixed for 15 min in ice-cold 4% PFA/PBS-CM, washed once in PBS-CM, permeabilized in 0.25% Triton X-100 / PBS-CM for 10 min, washed once in PBS-CM, blocked for 1 h at 37°C in Duolink blocking buffer (Sigma Aldrich) in a hyb oven, and incubated overnight at 4°C in mouse anti-puromycin plus the indicated rabbit antibody. The next day, cells were washed twice for five min in Duolink buffer A, then incubated for 1 h in hyb oven at 37°C in Duolink anti-mouse MINUS plus anti-rabbit PLUS probes diluted 1:5 in Duolink antibody dilution buffer. Cells were next washed twice for five min in buffer A, incubated for 30 min in hyb oven at 37°C in Duolink ligase diluted 1:40 in 1x ligation buffer, washed twice in buffer A, incubated for 100 min in hyb oven at 37°C in Duolink polymerase diluted 1:80 in 1x far r ed amplification buffer, washed twice for 10 min in buffer B, once in 1:100 buffer B / PBS-CM, once in PBS-CM, counterstained with DAPI, and embedded in mounting media. See Key Resources Table for complete list of antibodies and Duolink reagents.

cDNA constructs, oligonucleotides, and AAVs—See Key Resources table for complete list of recombinant cDNA constructs and oligonucleotide sequences.

Expression constructs encoding CMV-driven GFP_{NLS} alone, or GFP_{NLS} flanked by the 3' UTR endogenous to rat *Npas4* transcript variant XM_017588841.1 and *Npas4* short 5' UTR (NM_153626.1; i.e. 5' UTR_s-GFP_{NLS}), or 3' UTR and long 5' UTR of *Npas4* (XM_017588841.1; i.e. 5' UTR_L-GFP_{NLS}) were cloned by VectorBuilder Inc., Shenandoah, TX, USA.

dCas9-GFP was previously generated (Nelles et al., 2016), and obtained from Addgene. FL-*Npas4* encoded the 5' UTR, CDS (NM_153626.1), and 3' UTR of rat *Npas4* transcript variant XM_017588841.1 as a continuous open reading frame driven by a CMV promoter, and was generated by VectorBuilder Inc., Shenandoah, TX, USA. sgRNA constructs used in dCas9 experiments encoded variable spacer sequences and invariant stem loop structure sequence driven by a U6 promoter, and upstream of turboRFP driven by a CAG promoter. sgRNA spacer sequences were designed to target non-PAM-adjacent sequences of *Npas4* mRNAs overlapping with regions complementary to smFISH probes, and constructs were generated by VectorBuilder. PAMmer molecules were 27mer mixed DNA / 2-O-methyl RNA oligonucleotides including a PAM-mismatch, and were synthesized by Integrated DNA Technologies, Coraville, IA, USA. PAMmers were co-transfected into cells at 5 pM per well (cells were cultured in 24-well dishes) with cDNA constructs using Lipofectamine 2000, as described above. See Table S7 for sgRNA and PAMmer sequences.

A bicistronic construct encoding U6-driven sgRNA sequence and Cas9-GFP (PX458) was previously generated (Ran et al., 2013), and obtained from Addgene. The spacer sequences targeting rat *Npas4* (XM_017588841.1), rat *Arntl* (alias *Amt*; NM_012780.1), or rat *Arnt2* (NM_012781.3) genes were designed using CRISPRdirect (crispr.dbcls.jp; Naito et al., 2015 Bioinformatics, 31, 1120-1123). *Npas4*-targeting spacer sequences were cloned into PX458 by Genscript, Piscataway, NJ, USA. Dual spacer sequences targeting *Arnt1* or *Arnt2* were cloned into a tricistronic construct encoding U6-driven sgRNAs and CBh-driven Cas9-GFP_{NLS} by VectorBuilder Inc. See Table S7 for sgRNA sequences.

An viral expression vector encoding U6-driven sgRNA sequence and hSyn-driven GFP fused to the nuclear envelope protein KASH (pAAV-U6sgRNA(SapI)_hSyn-GFP-KASH-bGH; PX552) was previously generated (Swiech et al., 2015) and obtained from Addgene. The spacer sequences targeting analogous regions in the mouse *Npas4* gene (XM_011248619.2) as those targeting the rat gene were designed using CRISPRdirect, and cloned into PX552. Subsequently, sgRNA expression vectors were packaged into AAVs using capsid serotype 2.1 (alias AAV1) by VectorBuilder Inc., and AAVs injected into mouse hippocampus using sterotaxis as described above. See Table S7 for sgRNA sequences.

Single molecule fluorescence *in situ* hybridization (smFISH)—smFISH was performed using the RNAscope ISH Multiplex kit (Wang et al., 2012), and probes were purchased directly from Advanced Cell Diagnostics, Hayward, CA, USA (See Key Resources Table). Target probes were tagged and conjugated to fluorescent dyes: C1, AlexaFluor 488; C2, Atto 555; C3, Atto 647. All experimental steps were carried out under RNase-free conditions.

Tissue Sections: smFISH was performed according to the manufacturer's recommendations for tissue sections from mice. Briefly, mice were anesthetized with isoflurane prior to decapitation and removal of hippocampi. Hippocampi were fixed in RNase-free 4% PFA / PBS at 4°C for 2 h with gentle agitation, fixative washed out and replaced with 30% sucrose / PBS for 48 h at 40°C, and embedded in OCT at −80°C. Fresh-fixed hippocampi we re cryosectioned in the coronal plane at 20 μm, collected on Superfrost Plus glass slides and subsequently stored at −80°C until smFISH processing. Slides were first subjected to antigen retrieval by incubation in RNAscope Target Retrieval Reagents for 5 min at 99–100°C, washed twice in water, dehydrated with 50% e thanol, 70% ethanol, and 2x washes in 100% ethanol for 5 min each at RT, followed by incubation in Protease IV reagent for 30 min at 40°C. Hybridizati on with target probes was performed at 40°C for 2 h in a hybridization oven (Boekel Scientific), followed by wash and amplification steps according to the manufacturer's protocol. After wash and amplification steps, tissue was counterstained with DAPI, and mounted in Fluoromount G media. A positive control probe against the house keeping gene Ubc (C3), and negative control probe against a bacterial gene, dapB (C1), were purchased from Advanced Cell Diagnostics and were used as references for the signal intensity and background level in each channel.

Cultured cells: smFISH in dissociated hippocampal cultures was performed as above with modifications. Neurons (14–16 DIV) were stimulated as described above, media gently aspirated, replaced with 4% PFA / PBS, and incubated for 15 min at RT. Coverslips were then washed twice in PBS, incubated in 50% ethanol for 5 min, 70% ethanol for 5 min, two incubations in 100% ethanol for 5 and 10 min, respectively, 70% ethanol for 2 min, and a final wash in 50% ethanol for 10 min, all at RT. Next, coverslips were washed in PBS, then incubated in Protease III reagent (ACD cat. 322337) diluted in PBS at 1:15 for 10 min at RT. Protease / PBS was gently aspirated, coverslips washed 2x in PBS, and hybridization with target probes was performed at 40°C for 2 h in a hybridization oven (Boekel Scientific), followed by wash and amplification steps according to the manufacturer's protocol. After

wash and amplification steps, coverslips were processed for either for puro-PLA followed by immunocytochemistry (ICC), or ICC alone. Puro-PLA was performed as described above, but cells were additionally post-fixed for 10 min in ice-cold 4% PFA / PBS-CM, then washed in PBS, permeabilized in 0.25% Triton X-100 / PBS for 10 min at RT, washed in PBS, and incubated in 10% NGS / PBS for 1 h at RT to block non-specific antibody binding. Subsequently, coverslips were incubated 1% NGS / PBS containing diluted primary antibodies at 40°C overnight. The next day, coverslips were washed three times in PBS, incubated in 1% NGS / PBS containing diluted secondary antibodies for 1 h at RT, washed three times in PBS, counterstained in DAPI for 1 min at RT, and mounted on Superfrost plus glass slides in 5 μL of Fluoromount G media. Coverslips subjected to ICC alone, after smFISH, were processed as described above but post-fixation was omitted.

Acute Slices: Hippocampal slices were prepared, whole-cell current clamp recordings obtained and biocytin-labeling performed as described above, before smFISH steps, and all were carried out under RNase-free conditions. Physiology was performed using patch pipettes baked at 200°C for 2 h to eliminate potential RNase contamination. Upon completion of biocytin-labeling, slices were mounted on Superfrost Plus slides, and dried overnight at RT. The next day, slides were incubated at 60°C for 1 h, washed three times in wa ter, dehydrated in 50% ethanol, 70% ethanol, and 2x in 100% ethanol for 8 min each, and then allowed to dry while a hydrophobic barrier was drawn around the slices. Protease IV reagent was added over slices, incubated at 40°C for 1 h, and then washed twice in PBS at RT. N ext, hybridization with target probes was performed at 40°C for 2 h in a hybridization oven (Boekel Scientific), followed by wash and amplification steps according to the manufacturer's protocol. Slices were counterstained with DAPI for 5 min at RT, and coverslipped.

Biochemistry

Acute slice lysates: Acute slices were prepared and stimulation delivered as described above. Pipettes were slowly removed immediately after delivery of the tetanus or control stimulus, and slices allowed to recover for 5 or 60 min in ACSF before dissection. Slices were then transferred to a light dissection microscope, immersed in dissection media consisting of (in mM): 1 $CaCl_2$, 5 $MgCl_2$, 10 glucose, 4 KCl, 26 $NaHCO_3$, 218 sucrose, 1.3 NaH_2PO_4.H2O, 30 HEPES, and the CA1 region—spanning from the alveus to SLM between proximal (CA2 boundary) and distal (subiculum boundary) —removed. CA1 tissue was then transferred to a chilled microcentrifuge tube and immediately flash frozen in liquid nitrogen. CA1 tissue sections obtained for the same experimental condition were pooled within the same tube (typically 6 tissue sections per sample for Co-IP), and stored at −80°C after flash freezing until lysis. Tissue samples for a single experimental condition were obtained from ventral–dorsal acute slices from either hemisphere, and prepared from at least 2 separate mice per experimental replicate.

Hippocampal lysates: Mice were anesthetized and killed by decapitation as described above, hippocampi dissected, collected in a chilled microcentrifuge tube, and flash frozen in liquid nitrogen. Data for each experimental condition was obtained from at least 3 separate mice; lysate from a single hippocampus was used for each experimental replicate.

Cultured cell lysates: Neuronal maintenance media was aspirated, cells were gently washed twice in ice-cold PBS, lysis buffer was added, and cells were collected in a chilled microcentrifuge tube using a cell scraper (Corning Costar Cat#3008). Cells prepared from at least 3 separate cultures were used for each experimental condition and across experimental replicates.

Lysis, Immunoprecipitation, and western blotting: Slices, tissue, and cultured cells were harvested as described above, and lysed in ice cold immunoprecipitation lysis buffer containing the following (in mM): 50 Tris pH 7.6, 150 NaCl, 1 EDTA, 10% glycerol, 1% NP-40 alternative (Sigma Aldrich Cat#492016), 0.5% Triton X-100, and supplemented with 10 phenylmethanylsulfonate (PMSF) and 1 tablet of cOmplete mini protease inhibitor cocktail (Sigma Aldrich Cat#11836170001). Whole-cell lysates were subjected to further mechanical disruption by passage through a 26-gauge syringe 5–6 times. Lysates were cleared by centrifugation at 16,000g for 30 min at 4°C and the solubilized fraction of protein was used for all biochemical experiments. For IP assays, 20 μl of Protein A- or G-Dynabeads (ThermoFischer Scientific Cat#10007D) was washed once in lysis buffer, added to the lysates with 2 μg of the indicated antibody, and nutated overnight at 4°C. The next day, immobilized immunocomplexes were recovered by washing 4x with lysis buffer, and solubilized with loading buffer (4x Laemmli Buffer (Bio-Rad Cat#1610747) + 10% 2-mercaptoethanol). Five per cent of whole-cell lysates were loaded as input samples.

Proteins were separated by SDS-PAGE, analyzed by immunoblotting with the indicated antibodies and visualized using SuperSignal™ West Femto Maximum Sensitivity Substrate (ThermoFisher Scientific Cat# 34095) on a western blot imaging system (Azure Biosystems c300), and quantified using FIJI software (see Key Resources Table).

RNA-Immunoprecipitation (RNA-IP)—All steps were carried out under RNase-free conditions. HEK293T cells were grown to 70% confluency, transfected with the indicated recombinant cDNA constructs, and incubated for 24 h post-transfection. Media was aspirated, cells were washed in ice-cold PBS, cells were collected using a cell scraper in a chilled microcentrifuge tube, and washed once in PBS. Cells were pelleted by centrifugation at 200g for 5 min at 4°C, supernatant removed, and pellet resuspended in mild lysis buffer supplemented with protease inhibitor cocktail, DTT, and RNase-inhibitor (Imprint® RNA Immunoprecipitation Kit; see Key Resources Table). Lysates were gently vortexed, nutated at 4°C for 15 min, me chanically disrupted by passage through a 26 gauge syringe 5x, centrifuged at 16,100g for 20 min at 4°C, and supernatant collected for immunoprecipitation. Ten per cent volume of each lysate was collected for whole cell input samples. Supernatants were nutated overnight at 4°C with 20 μL of Protein A-coated beads and 4 μL of rabbit anti-GFP or rabbit normal IgG as a control (see Key Resources Table).

Immobilized immunocomplexes were recovered by washing 5x in RIP wash buffer, resuspended in RIP wash buffer, and TRIzol™ Reagent (ThermoFisher Scientific Cat#15596026) added to purify RNAs. Chloroform (Sigma Aldrich Cat#C2432) was added, samples were briefly vortexed, centrifuged at 16,100g for 10 min at 4°C, aqueous p hase removed and transferred to a new tube, linear acrylamide (Sigma Aldrich Cat#C2432), ammonium acetate (Sigma Aldrich Cat#09691), and 2-propanol (Sigma Aldrich Cat#I9516)

added, samples briefly vortexed, and incubated for 1 h at −80°C. Samples were then thawe d on ice, centrifuged at 16,100g for 10 min at 4°C, supernatant discarded, pellets washed twice in 80% ethanol, and air dried in a laminar flow hood for 1 h. After drying, pellets were resuspended in water, input samples were diluted 1:10 to 1% final concentration, all samples treated with amplification grade DNase I (Sigma Aldrich Cat#AMPD1-1KT) for 15 min at room temp, reactions stopped and samples heated at 70°C for 10 min before being placed on ice.

RNA-purified samples were next annealed to primers for reverse transcription. To each sample, 50 mM dNTPs and 70 μM Oligo(dT)23, Anchored primers (Sigma Aldrich Cat#O4387-.1ML) were added, primer-RNA mixed samples were briefly vortexed, heated at 65°C for 5 min, and cooled on ice. As a control for reverse transcription, additional input samples were incubated in water instead of dNTPs and primers (denoted as –RT in Figure S5). To each sample, SuperScript™ IV Reverse Transcriptase (ThermoFisher Scientific Cat#18090010) reagents were added, samples incubated at 55°C for 10 min, 8 0°C for 10 min, held at 4°C, RNA removed using RNase H, and cDNAs amplified by PCR using Phusion High-Fidelity DNA Polymerase (ThermoFisher Scientific Cat#F530L) and specific primers against *Npas4* or *Actb* (See Table S7 for primer oligonucleotide sequences). Amplicons were labeled by SYBR™ Safe DNA Gel Stain (ThermoFisher Scientific Cat#S33102) and separated by gel electrophoresis on a 2% agarose gel.

T7 Endonuclease digestion—HEK293T cells were maintained and transfected with the indicated recombinant cDNA constructs as described above. 24 h after transfection, cellular media was aspirated, cells were washed once in ice cold PBS, collected using a cell scraper into a chilled microcentrifuge tube, centrifuged at 5000g at 4°C for 5 min, supernatant removed, and cells lysed in QuickExtract DNA Extraction Solution (Epicentre Cat#QE09050) to isolate genomic DNA. Sample DNA was amplified by PCR using Phusion polymerase and specific primer sets against discrete regions of *Npas4* targeted by each sgRNA (See Table S7 for primer oligonucleotide sequences). Amplicons were purified using DNA Clean & Concentrator 5 kit (Zymo Research Cat#D4013), then denatured at 95°C for 10 min, and slowly reann ealed at 95–85°C (ramp rate −2°C / s) and 85–25°C (ramp rate −0.3°C / s) to form heteroduplexes. Heteroduplexed DNA was incubated with T7 endonuclease I (New England BioLabs Cat#M0302S; 0.5U per reaction) or reaction buffer as a control (denoted as –T7 in Figure S4) at 37°C for 1 h. Reaction was stopped using EDTA, DNA labeled using SYBR Safe stain, and separated by gel electrophoresis on a 2% agarose gel.

Confocal imaging—All slices and tissue sections were imaged using an Olympus Fluoview 1000 confocal microscope (×10 / 0.4, ×20 / 0.75, and ×60 / 1.42 (oil) plan-apochromat objectives; UC San Diego School of Medicine Microscopy and Histology Core). Identical acquisition parameters were used for all slices or tissue within a single experiment. For imaging the full somatodendritic axis of CA1 at 60x magnification, separate images were acquired and tiled under visual control using the NeuN or DAPI signal as a landmark. For confocal imaging of biocytin-labeled cells, Kohler illumination was used to optimize the position of the condenser and DIC polarizers, and scanned using a 488nm laser.

ChIP-seq—Twenty seven DIV rat hippocampal neurons were treated with (in μM): 1 TTX, 10 NBQX, and 10 CPP for 24 h. The next day, media was then replaced with the same (silenced, – Stim) or media with 50 μM PTX (stimulated, + Stim) and incubated for 2 h at 37°C.

ChIP-seq was essentially performed as described (Heinz et al., 2018), with modifications. Briefly, neuronal maintenance media was aspirated, 2 mM Disuccinimidyl glutarate (DSG; ThermoFisher Scientific Cat#20593) / PBS for 30 min at room temp with gentle agitation, followed by an additional 15 min with 16% PFA added to 1% final. The reactions were quenched by adding 2.625 M glycine to 125 mM final, incubated for 5 min, then 20% bovine serum albumin (BSA; Fisher Bioreagents Cat#BP9706-100) added to 1% final, the mixture of fixatives aspirated and replaced with ice-cold 0.5% BSA / PBS, cells collected using a cell scraper into a chilled 15 mL conical tube, and centrifuged at 5000g for 5 min at 4°C.

Cells were resuspended in ice-cold LB3 lysis buffer containing the following (in mM) (10 Tris / HCl pH 7.5, 100 NaCl, 0.5 EGTA, 0.1% deoxycholate, 0.5% sarkosyl, 1× protease inhibitor cocktail (Sigma Aldrich Cat# P8340) and chromatin was sheared to an average DNA size of 300–500 bp by administering 7 pulses of 10 sec duration at 13 W power output with 30 sec pause on wet ice using a Misonix 3000 sonicator. The lysate was diluted in 1.1-fold (LB3) with ice-cold 10% Triton X-100. One per cent of the lysate was removed for whole cells inputs. For each immunoprecipitation, aliquots of lysate equivalent to 3_X10^6 cells for transcription factor and RNAPII antibodies, or 7.5_X10^5 cells for histone modification antibodies, 20 μl of Dynabeads Protein A (for rabbit polyclonal antibodies) or Dynabeads protein G (for murine monoclonal antibodies) and 2 μg of the indicated antibody were combined, and rotated overnight at 8 RPM and 4°C.

The next day, beads were collected on a magnet and washed 3x each with wash buffer I (WB1; in mM: 10 Tris / HCl pH 7.5, 150 NaCl, 1% Triton X-100, 0.1% SDS, 2 EDTA), wash buffer III (WB3; in mM: 10 Tris / HCl pH 7.5, 250 LiCl, 1 EDTA, 1% Triton X-100, 0.7% Deoxycholate) and 2x with ice-cold TET (in mM: 10 Tris / HCl pH 7.5, 1 EDTA, 0.025% Tween-20). Beads were then resuspended in 20μL cold TT (in mM: 10 Tris / HCl pH 7.5, 0.025% Tween-20).

Libraries were prepared with NEBNext Ultra II DNA library prep kit reagents according to the manufacturer's protocol on the beads suspended in TT, with reagent volumes reduced by half. ChIP samples were indexed by ligation to NEXTflex DNA Barcodes. DNA was eluted and crosslinks reversed by adding 4 μl 10% SDS, 4.5 μl 5 M NaCl, 3 μl EDTA, 1 μl proteinase K (20 mg / ml), 20 μl water, incubating for 1 h at 55°C, then 30 min to overnight at 65°C. DNA was cleaned up by adding 2 μl SpeedBeads 3 EDAC (Sigma Aldrich Cat#GE65152105050250) in 61 μl of 20% PEG 8000 / 1.5 M NaCl, mixing and incubating for 10 min at RT. SpeedBeads were collected on a magnet, washed twice by adding 150 μl 80% EtOH for 30 seconds each, collecting beads and aspirating the supernatant. After air-drying the SpeedBeads, DNA was eluted in 25 μl TT and the DNA contained in the eluate was amplified for 12 cycles in 50 μl PCR reactions using NEBNext Ultra II Q5 PCR master mix (New England BioLabs Cat#M0544S) and 0.5 μM each of primers Solexa 1GA and

Solexa 1GB (See Key Resources table). Libraries were cleaned up as above by adding 36.5 µl 20% PEG 8000 / 2.5 M NaCl and 2 µl Speedbeads, two washes with 150 µl 80% EtOH for 30 sec each, air-drying beads and eluting the DNA into 20 µl TT.

ChIP library size distributions were estimated following 2% agarose / TBE gel electrophoresis of 2 µl library, and library DNA amounts measured using a Qubit HS dsDNA kit on a Qubit fluorometer. ChIP input material (1% of sheared DNA) was treated with RNase for 15 min at 37°C in EB buffer (in mM: 10 Tris pH 8, 5 EDTA, 280 NaCl, and 0.5% SDS), then digested with Proteinase K for 1 h at 55°C and crosslinks reverse d at 65°C for 30 min to overnight. DNA was cleaned up with 2 µl SpeedBeads 3 EDAC in 61 µl of 20% PEG 8000 / 1.5 M NaCl and washed with 80% ethanol as described above. DNA was eluted from the magnetic beads with 25 µl of TT and library prep and amplification were performed as described for ChIP samples.

The antibodies used are listed in the Key Resources Table. Libraries were sequenced singleend for a minimum of 84bp and 8bp for each index to a depth of 15–20 million reads on an Illumina NextSeq 500 instrument.

RNA-seq—RNA-seq was performed as previously described (Heinz et al., 2018). Briefly, DIV 27 hippocampal neurons were silenced or stimulated exactly as described for ChIP-seq experiments, lysed the next day in TRI-reagent and RNA was extracted using a Direct-zol kit (Zymo Research Cat#R2051) with on-column DNase treatment, following the manufacturer's instructions. Strand-specific total RNA-seq libraries from ribosomal RNA-depleted RNA were prepared using the TruSeq kit Stranded Total RNA Library kit (Illumina) according to the manufacturer-supplied protocol. Library construction was performed by the IGM Genomics Center, University of California, San Diego, La Jolla, CA. Libraries were sequenced single-end for a minimum of 76 bp for each index to a depth of approximately 40 million host genome reads on an Illumina NextSeq 500 instrument.

Quantification and Statistical Analysis

Physiology Data Acquisition and Analysis—Recordings were obtained with a Multiclamp 700B, and a National Instruments data acquisition board (NI PCIe-6259 and BNC-2110) under the control of a Windows 7-based 32-bit computer equipped with MATLAB software (MathWorks Inc.) running ScanImage (Pologruto et al., 2003). Extracellular stimuli were delivered by current injection under the control of ScanImage, delivered through a National Instruments stimulus board (NI PCIe-6733 and BNC-2110), and amplitude was adjusted through a stimulus isolator (A.M.P.I. ISO-Flex). Data were sampled at 10 kHz and filtered at 4 or 6 kHz. Off-line data analysis was performed using custom software written in Igor Pro (Wavemetrics Inc.) by B.L.B. and A.L.H. (Bloodgood et al., 2013).

The amplitude of EPSPs was calculated using custom written software in Igor Pro (A.L.H.; (Hartzell et al., 2018). Briefly, the baseline membrane potential was averaged from 0–98 ms before delivery of the stimulus pulse at 100 ms, and the peak amplitude between 2–20 ms post-stimulus was quantified relative to baseline. For stimulation in SLM, EPSP amplitude was quantified from 2–50 ms post-stimulus.

Image Analysis and Quantification—Confocal images for a particular experiment were subjectively thresholded using the Fiji package of ImageJ (Schindelin et al., 2012; Schneider et al., 2012), and the same threshold was used for all images obtained for a single experiment, throughout the experimental analysis. Puncta were defined as a thresholded fluorescence cluster with an area ≥ 0.05 μm^2. Puncta number and integrated density (the product of area and mean grey value, termed immunohistofluorescence, IHF) were then determined using Fiji. For quantification of NPAS4 IHF in acute slices, confocal images of slices obtained from *Npas4*$^{-/-}$ mice were analyzed and thresholded, and the same threshold (60–255; 8-bit scale) was applied to stimulated slices from WT mice throughout all acute slice experiments. To selectively analyze fluorescence in specific cellular lamina, the NPAS4 channel was overlaid onto the NeuN channel in Fiji, and NeuN signal was used to delineate the different layers.

To reconstruct cellular morphology using biocytin labeling, a maximum intensity projection of the DIC images was generated in Fiji. A thresholded mask of cell's outline was then created using the Fiji magic wand tool. At high magnification in Photoshop CC software, the contours generated by the Fiji magic wand tool were traced using the Photoshop pencil tool and then overlaid onto the fluorescence image panels in the figures, where indicated.

Confocal images obtained at 60x magnification along the somato-dendritic axis of CA1 were acquired separately using identical acquisition parameters, then tiled using NeuN or DAPI as landmarks as described above. Levels, contrast, and brightness were moderately and separately adjusted for each channel of each image in Photoshop CC, using identical parameters across images of a single region of interest in hippocampal CA1. Images were overlaid in Illustrator CC using the screen transparency setting, positioned until NeuN or DAPI landmarks completely overlapped, and then composites of the overlaid images were presented in the figures (shown in Figures 1A, 1F, 2J, 2L, 2O, 3B, 3D, S1I, S3N-Q, S3S, S5G, S6B, and S6D). Clipping masks were occasionally used to crop regions of images for positioning within figures, or for overlaying biocytin morphology reconstructions at high magnifications.

Quantification of mRNA puncta number in tissue and slices was performed in Fiji using 10 μm bins to count thresholded puncta, beginning at the superficial edge of SO, and continuing through the tiled images to the border of SLM and the dentate gyrus, encompassing a total of 400 μm. Area under the curve (AUC) was quantified using a trapezoidal formula (AUC = ΔX*(Y1+Y2)/2) in Prism software (Graphpad Inc., La Jolla, CA), where all Y values >0 ($Y_{baseline}$ = 0.0) were considered for x values defined by borders of hippocampal lamina, relative to superficial edge of SP at border with SR: SO (−200–100 μm), SP (−100–0 μm), SR (0–200 μm), and SLM (200–400 μμm).

Quantification of mRNA puncta number or protein intensity (mean gray value, 8-bit scale) in cultured neurons as function of concentric distance from the nucleus was performed using Fiji and SynD image analysis package (Schmitz et al., 2011) running in MATLAB. To quantify mRNA or protein localized to a transfected cell's nucleus, *Npas4* mRNA, puro-PLA–labeled NPAS4 or GFP, or NPAS4 protein fluorescence signal was thresholded in Fiji, as described above, and puncta number or intensity were analyzed within a region of interest

(ROI) outlining DAPI counterstain, or GFP_{NLS}. Quantification of puncta within the cell soma, excluding fluorescence within the nucleus, was analyzed within a ROI outlining the cell soma, defined by the transfected fluorescent protein filling cellular morphology (e.g. RFP) or at the boundary of immunofluorescent MAP2 signal, and which excluded the ROI outlining DAPI. Quantification of puncta within dendrites as a function of increasing distance from nucleus and soma was performed in SynD. Following thresholding of RFP cell fill channel, or GFP_{NLS} merged with MAP2 immunofluorescence, and NPAS4 channel in Fiji, a mask of RFP or GFP_{NLS} + MAP2 was created to outline the morphology of the transfected cell, overlaid on to the NPAs4 channel, and exported as a single TIFF image. The RFP mask of transfected cell morphology was overlaid on the other channels in the images shown in Figure S5D, F. The overlaid TIFF image was opened in SynD, fluorescent signal from RFP or GFP_{NLS} + MAP2 was assigned to channel 1 (morphology), and mRNA, puro-PLA, or protein fluorescence assigned to channel 2 (synapses). Channel 3 was not used. Cell soma was detected using default settings, somatic signal removed, and dendrites detected using default filter size. mRNA or puro-PLA puncta number along dendrites were counted as “synapses” and NPAS4 protein intensity was counted as “syn (mean)” value. Among all cells imaged, nuclei and soma exhibited diameters of 8 μm and 15 μm, respectively and on average, and so dendritic puncta were quantified along concentric radial distance from center of nucleus beginning at 9 μm, and up to 50 μm. AUC for dendritic puncta was quantified as described above, and expressed in Figure 4 as puncta number × μm for mRNA, or puncta intensity × μm for protein.

Western Blot Analysis—Acquired blot images were opened in Fiji, converted to 8-bit, and rectangular tool used to vertically outline each lane in its entirety for the gel analysis routine. The relative intensity of each lane was quantified using the plot lanes tool, peaks corresponding to protein bands were closed using the straight line tool to account for background signal, and peak area and percent were quantified using the wand tool. The relative intensity of each band was determined by normalizing first to a loading control (β-actin bands in input blots, and IP’d protein bands in Co-IP blots), and then to a defined experimental control lane within a particular gel (lane corresponding to unstimulated or first time point samples in input blots, and IgG lanes in Co-IP experiments). Blot images shown in figures were cropped horizontally from the full length blot around all bands detected by the indicated antibody at the protein’s predicted molecular weight, consistent with those reported in the literature, and were uniformly adjusted for brightness and contrast to enhance signal visibility within the figure. The NPAS4 blot shown in Fig. S7B was cropped vertically at the border between the 5% input lanes and IgG lanes, contrast and brightness adjusted differentially to account for differences in input protein and IP’d protein levels, and the two cropped images were spliced back together within the figure, with a dashed vertical line denoting the splice site.

ChIP-seq Analysis—Reads were first filtered for quality (QC>20) and length (>15bp) and adapter sequences were removed with FASTP (Chen et al., 2018) using default settings. Reads were then mapped with Bowtie2 (Langmead and Salzberg, 2012) to the rat genome (RGSC 6.0/rn6) using –very-sensitive-local -N 1 and otherwise default settings. Alignment files were converted to BAM files, sorted, indexed, and marked for read duplicates with

samTools (Li et al., 2009). The quality of each ChIP-seq sample was gauged by the synthetic JS-distance metric (Figure S6E) as output by the plotFingerprint command with --ignoreDuplicates --extendReads 150 options from deepTools (Ramirez et al., 2014).

Individual replicate alignment files for each ChIP and condition were concatenated. BAM files were further processed into tag directories for analysis with HOMER (Heinz et al., 2010) using the makeTagDirectory command with the -fragLength 150 option. ChIP-seq peaks were called with HOMER's findPeaks program in "factor" (NPAS4, ARNT1, ARNT2) mode with a peak size of 350 base-pairs, condition-matched inputs, and otherwise default settings. HOMER was also used to generate sequencing-depth normalized bedGraph/bigWig files for visualization in the UCSC Genome Browser (Figures 6H and 7H-I) (Bailey et al., 2002).

Because cultured neurons had some baseline activation even when pharmacologically silenced, reads from both silenced and stimulated NPAS4 ChIPs were counted at stimulated NPAS4 peaks using HOMER's annotatePeaks.pl tool with the -d option, and these peaks filtered against signal in the silenced NPAS4 ChIP. Only peaks with less than 40 reads (normalized to 10 million total reads) in the silenced condition and greater than 3-fold increases in the stimulated condition relative to the silenced condition were kept. This filtered NPAS4 peak-set was used for all downstream analysis involving NPAS4 peaks (with the exception of the scatter plot in Figure 6A, which was made using the set of all NPAS4 peaks in both silenced and stimulated conditions). All scatterplots of $\log_2$ tag counts (Figure 6A-C) were made in Microsoft Excel using the file output by HOMER's annotatePeaks.pl tool with -log and -d options. Where peaks from both silenced and stimulated conditions were used (Figure 6A-C) HOMER's mergePeaks tool was used with default settings to combine peak-sets. All aggregate histograms (Figure 6D, E) were produced in Microsoft Excel using the output from annotatePeaks.pl with -hist 5, -size 3000, and -d options. Genome annotations (Figures 6H and 7G-I) for NPAS4 peaks were produced using HOMER's annotatePeaks.pl tool with the rn6 reference genome and otherwise default settings, and peaks were filtered on the following annotation criteria to create pie charts: annotation containing 'TSS', 'CpG', 'intron' or 'exon' and not 'CpG' (intragenic), and 'intergenic' and not 'CpG' (intergenic).

Filtered NPAS4 peaks were sorted by the $\log_2$ ratio of ARNT1 to ARNT2 ($\log_2(ARNT1_{PTX}/ARNT2_{PTX})$) ChIP-seq read counts from stimulated cells within each peak and annotated by quartile along this ratio. This sorted and quartile annotated peak list was then formatted according to the deepTools fileSortedRegions format and used as the reference file to make a coverage matrix of NPAS4, ARNT1, ARNT2, H3K27ac, and RNAPII ChIPs using deepTools' computeMatrix tool in reference-point mode with the --referencePoint center option and bigwigs of the above ChIPs (made from BAM files using the bamCoverage command from deepTools with -bs 1, --normalizeUsing BPM, and --extendReads 150 options) as input. This coverage matrix was plotted as a heatmap using plotHeatmap with --interpolationMethod 'bilinear' and --sortRegions keep options (Figure 6G).

HOMER's findMotifsGenome.pl tool was used to find *de novo* enriched motifs within the above quartiles of NPAS4 peaks using the rn6 reference genome and -size 350 (Figure S7).

To compare and visualize enrichment of top *de novo* motifs along a finer gradient of the ARNT1:ARNT2 ratio, NPAS4 peaks were further split into deciles along the ARNT1:ARNT2 ratio. Motif files of the top 5 non-redundant motifs from each quartile were combined and used as input for the -mknown option of findMotifsGenome.pl, again using the rn6 reference genome, - size 350, and the NPAS4 peak deciles used as the peak file input. The ratio of percentage of target regions to background regions with each of the de novo motifs was then plotted as a heatmap using seaborn's clustermap function (Figure 6I; Waskom et al., 2018).

To verify enrichment of *de novo* motifs across the continuum of the ARNT1:ARNT2 ratio, we performed a logistic regression of motif presence in peak sequences over ARNT1:ARNT2 ratios. In order to control for the effect of dinucleotide frequency bias on motif enrichment, we derived 11 principal components from the dinucleotide frequencies that explained at least 99.0% of the variance in those frequencies. These principal components were then used as covariates for the logistic regression model. Then for each motif, the logistic regression model was fit for presence of that motif in each sequence, over the ARNT1:ARNT2 ratios and covariates. ARNT1:ARNT2 ratios and covariates were then normalized to facilitate convergence in the logistic regression model estimation. This yielded a regression coefficient for each motif describing the change in $\log_{10}$ odds of a peak containing the motif, per standard deviation change in ARNT1:ARNT2, after controlling for dinucleotide composition. Significance of this coefficient was determined using the Wald test p-value, after multiple testing corrections. This implementation is publicly available as MEIRLOP at (https://github.com/npdeloss/meirlop).

RNA-seq analysis—In order to determine genes differentially expressed across conditions, we preprocessed reads using FastP, removing adapter sequences, then aligned using STAR to the ENCODE Rnor 6.0 genome (Dobin et al., 2013). We then used HOMER to create tag directories and quantify read counts over rn6 RefSeq transcripts. DESeq2 was then used to call differentially expressed genes from the counts, using the getDiffExpression.pl script from HOMER (Love et al., 2014). Gene ontology analysis was performed with differential expression lists using Metascape (Zhou et al., 2019).

In order to assess relative co-occupancy of ARNT1 or ARNT2 at NPAS4 peaks in the vicinity of up-regulated genes in stimulated cells, we plotted distributions of ARNT1:ARNT2 signal ratios at NPAS4 surrounding genes. Bedmap from the bedops suite was used to assign NPAS4 peaks within variable distances on a $\log_{10}$ scale ($< 10^2$, $< 10^3$, $< 10^4$, $>10^4$) from TSS of up-regulated genes to their respective genes (Neph et al., 2012). Sequencing-depth normalized tag counts of ARNT1 and ARNT2 at NPAS4 peaks were summed for each TSS. For each of these TSS-to-peak distances, the distribution of the ARNT1/ARNT2 ratio of each gene was plotted, arranging distributions for each distance into a ridge-plot and violin plot using Seaborn (Figure 7).

Statistical Analysis—Mean ± S.E.M. is used as an estimate of center and dispersion of data values throughout the paper, with the exception ChIP-seq experiments where individual data points are scatter-plotted on a $\log_2$ scale, or aggregate-plotted and normalized to the indicated control condition. For all electrophysiology, IHC, smFISH experiments, 'n' refers

to the number of cells recorded, slices, tissue sections, or cells used per condition, and obtained from a specified number of separate mice, respectively. For biochemistry experiments in Figure 5, 'n' refers to the number of independent experimental replicates performed, obtained from a specified number of separate mice. Our sample sizes were not pre-determined, and are similar to those reported in the literature. Data collection and analysis were not performed blind to the conditions of the experiment and were not acquired with any specific randomization procedure. However, experimental subjects were assigned to experimental groups and analysis was performed with absolutely no bias, and by different experimenters. Statistical analysis was performed in Prism software (GraphPad Inc.) and did not meet the assumption of normality (D'Agostino and Pearson omnibus normality test), and so non-parametric statistical tests were performed, with the exception of biochemistry experiments in Figure 5 and S7 where the "n" value was too small, and so normal distributions were assumed and parametric tests were performed. However, in experiments involving ≥ 2 independent variables, no appropriate non-parametric test was available, so two-way analysis of variance (ANOVA) with *post-hoc* tests were performed. For analysis of normalized reads of ARNT1 vs ARNT2 peaks at NPAS4 peaks (Figure S6G), 'n' refers to the number of individual peaks, and data did not meet the assumption of normality. For analysis of the cumulative fraction of $\log_2(ARNT1_{PTX}/ARNT2_{PTX})$ values at NPAS4 peaks assigned to activity-upregulated genes in stimulated cells (Figure 7D), 'n' refers to the number of individual peaks assigned to the indicated bins of distance from gene TSS, and did not meet the assumption of normality. Statistical analysis of ChIP-seq and RNA-seq data was otherwise performed as described above. Statistical significance was determined by Mann-Whitney U-test, Kruskal-Wallis test with *post-hoc* tests, one-way or two-way ANOVA with *post hoc* tests, or twoway student's t-test with Welch's correction using Prism software, where indicated in Table S1. Statistical significance was assumed when $P<0.05$. In all figures, *$P<0.05$, **$P<0.01$ and ***$P<0.001$ as determined in Prism software. The statistical details of all experiments (with the exception of some ChIP-seq experiments), including 'n' values and definitions, P values, and data variability estimates are found in Table S1, and itemized according to figure panel for main figures and supplemental figures. All figures were generated using Illustrator CC software (Adobe Systems, Inc.).

Data and Software Availability

The accession numbers for ChIP-seq and RNA-seq data from primary cultured neurons reported in this paper are NCBI GSE127793 and GSE134203, respectively. Analysis software developed for ChIP-seq experiments in this study are detailed above, and included in HOMER, available at http://homer.ucsd.edu/homer/.

Supplementary Material

Refer to Web version on PubMed Central for supplementary material.

ACKNOWLEDGEMENTS:

This work was supported by grants from the Pew Charitable Trust (00028631), Kinship Foundation/Searle Scholars Program (14-SSP-184), and Whitehall Foundation (2013-12-88) (B.L.B.), NIMH (F32MH110141; G.S.B), the NLM Training Grant (T15LM011271; N.P.D.S.), and NSF (2015215385; P-A.L.). J.R.E. is an HHMI Investigator. The UCSD School of Medicine Microscopy and Histology Core is supported by NINDS (NS047101). We thank:

Gene W. Yeo, David A. Nelles, and Frederick E. Tan (UCSD) for the gift of pcDNA3.1-dCas9-2xNLS-EGFP and for technical input on dCas9 experiments; Byungkook Lim (UCSD) for assistance with AAV packaging; Gentry N. Patrick and Lara Dozier (UCSD) for providing cultures; Damian G. Wheeler (Activity Signaling Inc.) for the gift of NPAS4 antibody. PX458 and PX552 plasmids were gifts from Feng Zhang (Broad Institute, MIT) and obtained from Addgene.

REFERENCES AND NOTES:

Bailey JA, Gu Z, Clark RA, Reinert K, Samonte RV, Schwartz S, Adams MD, Myers EW, Li PW, and Eichler EE (2002). Recent segmental duplications in the human genome. Science 297, 1003–1007. [PubMed: 12169732]

Bartel DP, Sheng M, Lau LF, and Greenberg ME (1989). Growth factors and membrane depolarization activate distinct programs of early response gene expression: dissociation of fos and jun induction. Genes Dev 3, 304–313. [PubMed: 2498163]

Bersten DC, Sullivan AE, Peet DJ, and Whitelaw ML (2013). bHLH-PAS proteins in cancer. Nat Rev Cancer 13, 827–841. [PubMed: 24263188]

Bloodgood BL, Sharma N, Browne HA, Trepman AZ, and Greenberg ME (2013). The activity-dependent transcription factor NPAS4 regulates domain-specific inhibition. Nature 503, 121–125. [PubMed: 24201284]

Buckle PJ, and Haas HL (1982). Enhancement of synaptic transmission by 4-aminopyridine in hippocampal slices of the rat. J Physiol 326, 109–122. [PubMed: 6286946]

Burgin KE, Waxham MN, Rickling S, Westgate SA, Mobley WC, and Kelly PT (1990). In situ hybridization histochemistry of Ca2+/calmodulin-dependent protein kinase in developing rat brain. J Neurosci 10, 1788–1798. [PubMed: 2162385]

Burmeister SS, Jarvis ED, and Fernald RD (2005). Rapid behavioral and genomic responses to social opportunity. PLoS Biol 3, e363. [PubMed: 16216088]

Cajigas IJ, Tushev G, Will TJ, tom Dieck S, Fuerst N, and Schuman EM (2012). The local transcriptome in the synaptic neuropil revealed by deep sequencing and high-resolution imaging. Neuron 74, 453–466. [PubMed: 22578497]

Ch'ng TH, DeSalvo M, Lin P, Vashisht A, Wohlschlegel JA, and Martin KC (2015). Cell biological mechanisms of activity-dependent synapse to nucleus translocation of CRTC1 in neurons. Front Mol Neurosci 8, 48. [PubMed: 26388727]

Ch'ng TH, Uzgil B, Lin P, Avliyakulov NK, O'Dell TJ, and Martin KC (2012). Activity-dependent transport of the transcriptional coactivator CRTC1 from synapse to nucleus. Cell 150, 207–221. [PubMed: 22770221]

Chang TH, Huang HY, Hsu JB, Weng SL, Horng JT, and Huang HD (2013). An enhanced computational platform for investigating the roles of regulatory RNA and for identifying functional RNA motifs. BMC bioinformatics 14 Suppl 2, S4.

Chen LF, Lin YT, Gallegos DA, Hazlett MF, Gomez-Schiavon M, Yang MG, Kalmeta B , Zhou AS, Holtzman L, Gersbach CA, et al. (2019). Enhancer Histone Acetylation Modulates Transcriptional Bursting Dynamics of Neuronal Activity-Inducible Genes. Cell reports 26, 1174–1188 e1175. [PubMed: 30699347]

Chen S, Zhou Y, Chen Y, and Gu J (2018). fastp: an ultra-fast all-in-one FASTQ preprocessor. Bioinformatics 34, i884–i890. [PubMed: 30423086]

Chiou SH, Winters IP, Wang J, Naranjo S, Dudgeon C, Tamburini FB, Brady JJ, Yang D, Gruner BM, Chuang CH, et al. (2015). Pancreatic cancer modeling using retrograde viral vector delivery and in vivo CRISPR/Cas9-mediated somatic genome editing. Genes Dev 29, 1576–1585. [PubMed: 26178787]

Cochran BH (1993). Regulation of immediate early gene expression. NIDA Res Monogr 125, 3–24. [PubMed: 8341367]

Cole AJ, Saffen DW, Baraban JM, and Worley PF (1989). Rapid increase of an immediate early gene messenger RNA in hippocampal neurons by synaptic NMDA receptor activation. Nature 340, 474–476. [PubMed: 2547165]

Coutellier L, Beraki S, Ardestani PM, Saw NL, and Shamloo M (2012). Npas4: a neuronal transcription factor with a key role in social and cognitive functions relevant to developmental disorders. PLoS One 7, e46604. [PubMed: 23029555]

Creyghton MP, Cheng AW, Welstead GG, Kooistra T, Carey BW, Steine EJ, Hanna J, Lodato MA, Frampton GM, Sharp PA, et al. (2010). Histone H3K27ac separates active from poised enhancers and predicts developmental state. Proc Natl Acad Sci U S A 107, 21931–21936. [PubMed: 21106759]

Darzacq X, Shav-Tal Y, de Turris V, Brody Y, Shenoy SM, Phair RD, and Singer RH (2007). In vivo dynamics of RNA polymerase II transcription. Nat Struct Mol Biol 14, 796–806. [PubMed: 17676063]

Djakovic SN, Marquez-Lona EM, Jakawich SK, Wright R, Chu C, Sutton MA, and Patrick GN (2012). Phosphorylation of Rpt6 regulates synaptic strength in hippocampal neurons. J Neurosci 32, 5126–5131. [PubMed: 22496558]

Dobin A, Davis CA, Schlesinger F, Drenkow J, Zaleski C, Jha S, Batut P, Chaisson M, and Gingeras TR (2013). STAR: ultrafast universal RNA-seq aligner. Bioinformatics 29, 15–21. [PubMed: 23104886]

Felsenstein J, and Churchill GA (1996). A Hidden Markov Model approach to variation among sites in rate of evolution. Mol Biol Evol 13, 93–104. [PubMed: 8583911]

Feng G, Mellor RH, Bernstein M, Keller-Peck C, Nguyen QT, Wallace M, Nerbonne JM, Lichtman JW, and Sanes JR (2000). Imaging neuronal subsets in transgenic mice expressing multiple spectral variants of GFP. Neuron 28, 41–51. [PubMed: 11086982]

Ghosh A, Ginty DD, Bading H, and Greenberg ME (1994). Calcium regulation of gene expression in neuronal cells. J Neurobiol 25, 294–303. [PubMed: 7910846]

Giorgi C, Yeo GW, Stone ME, Katz DB, Burge C, Turrigiano G, and Moore MJ (2007). The EJC factor eIF4AIII modulates synaptic strength and neuronal protein expression. Cell 130, 179–191. [PubMed: 17632064]

Gorski JA, Talley T, Qiu M, Puelles L, Rubenstein JL, and Jones KR (2002). Cortical excitatory neurons and glia, but not GABAergic neurons, are produced in the Emx1-expressing lineage. J Neurosci 22, 6309–6314. [PubMed: 12151506]

Greenberg ME, and Ziff EB (1984). Stimulation of 3T3 cells induces transcription of the c-fos proto-oncogene. Nature 311, 433–438. [PubMed: 6090941]

Guschin DY, Waite AJ, Katibah GE, Miller JC, Holmes MC, and Rebar EJ (2010). A rapid and general assay for monitoring endogenous gene modification. Methods Mol Biol 649, 247–256. [PubMed: 20680839]

Hartzell AL, Martyniuk KM, Brigidi GS, Heinz DA, Djaja NA, Payne A, and Bloodgood BL (2018). NPAS4 recruits CCK basket cell synapses and enhances cannabinoid-sensitive inhibition in the mouse hippocampus. Elife 7.

Heinz S, Benner C, Spann N, Bertolino E, Lin YC, Laslo P, Cheng JX, Murre C, Singh H, and Glass CK (2010). Simple combinations of lineage-determining transcription factors prime cis-regulatory elements required for macrophage and B cell identities. Mol Cell 38, 576–589. [PubMed: 20513432]

Heinz S, Texari L, Hayes MGB, Urbanowski M, Chang MW, Givarkes N, Rialdi A, White KM, Albrecht RA, Pache L, et al. (2018). Transcription Elongation Can Affect Genome 3D Structure. Cell 174, 1522–1536 e1522. [PubMed: 30146161]

Hinnebusch AG, Ivanov IP, and Sonenberg N (2016). Translational control by 5'-untranslated regions of eukaryotic mRNAs. Science 352, 1413–1416. [PubMed: 27313038]

Joo JY, Schaukowitch K, Farbiak L, Kilaru G, and Kim TK (2016). Stimulus-specific combinatorial functionality of neuronal c-fos enhancers. Nat Neurosci 19, 75–83. [PubMed: 26595656]

Ju W, Morishita W, Tsui J, Gaietta G, Deerinck TJ, Adams SR, Garner CC, Tsien RY, Ellisman MH, and Malenka RC (2004). Activity-dependent regulation of dendritic synthesis and trafficking of AMPA receptors. Nat Neurosci 7, 244–253. [PubMed: 14770185]

Kewley RJ, Whitelaw ML, and Chapman-Smith A (2004). The mammalian basic helix-loop-helix/PAS family of transcriptional regulators. Int J Biochem Cell Biol 36, 189–204. [PubMed: 14643885]

Kieft JS (2008). Viral IRES RNA structures and ribosome interactions. Trends in biochemical sciences 33, 274–283. [PubMed: 18468443]

Kim TK, Hemberg M, Gray JM, Costa AM, Bear DM, Wu J, Harmin DA, Laptewicz M, Barbara-Haley K, Kuersten S, et al. (2010). Widespread transcription at neuronal activity-regulated enhancers. Nature 465, 182–187. [PubMed: 20393465]

Kislauskis EH, Zhu X, and Singer RH (1994). Sequences responsible for intracellular localization of beta-actin messenger RNA also affect cell phenotype. J Cell Biol 127, 441–451. [PubMed: 7929587]

Kosik KS (2016). Life at Low Copy Number: How Dendrites Manage with So Few mRNAs. Neuron 92, 1168–1180. [PubMed: 28009273]

Kozak M (1987). An analysis of 5'-noncoding sequences from 699 vertebrate messenger RNAs. Nucleic Acids Res 15, 8125–8148. [PubMed: 3313277]

Langmead B, and Salzberg SL (2012). Fast gapped-read alignment with Bowtie 2. Nat Methods 9, 357–359. [PubMed: 22388286]

Le SY, and Maizel JV Jr. (1997). A common RNA structural motif involved in the internal initiation of translation of cellular mRNAs. Nucleic Acids Res 25, 362–369. [PubMed: 9016566]

Li H, Handsaker B, Wysoker A, Fennell T, Ruan J, Homer N, Marth G, Abecasis G, Durbin R, and Genome Project Data Processing, S. (2009). The Sequence Alignment/Map format and SAMtools. Bioinformatics 25, 2078–2079. [PubMed: 19505943]

Lin Y, Bloodgood BL, Hauser JL, Lapan AD, Koon AC, Kim TK, Hu LS, Malik AN, and Greenberg ME (2008). Activity-dependent regulation of inhibitory synapse development by Npas4. Nature 455, 1198–1204. [PubMed: 18815592]

Lipton JO, Yuan ED, Boyle LM, Ebrahimi-Fakhari D, Kwiatkowski E, Nathan A, Guttler T, Davis F, Asara JM, and Sahin M (2015). The Circadian Protein BMAL1 Regulates Translation in Response to S6K1-Mediated Phosphorylation. Cell 161, 1138–1151. [PubMed: 25981667]

Love MI, Huber W, and Anders S (2014). Moderated estimation of fold change and dispersion for RNA-seq data with DESeq2. Genome biology 15, 550. [PubMed: 25516281]

Ma H, Groth RD, Cohen SM, Emery JF, Li B, Hoedt E, Zhang G, Neubert TA, and Tsien RW (2014). gammaCaMKII shuttles Ca(2)(+)/CaM to the nucleus to trigger CREB phosphorylation and gene expression. Cell 159, 281–294. [PubMed: 25303525]

Madabhushi R, Gao F, Pfenning AR, Pan L, Yamakawa S, Seo J, Rueda R, Phan TX, Yamakawa H, Pao PC, et al. (2015). Activity-Induced DNA Breaks Govern the Expression of Neuronal Early-Response Genes. Cell 161, 1592–1605. [PubMed: 26052046]

Magee JC, and Johnston D (1995). Synaptic activation of voltage-gated channels in the dendrites of hippocampal pyramidal neurons. Science 268, 301–304. [PubMed: 7716525]

Magee JC, Johston Daniel (1995). Characterization of single voltage-gated Na+ and Ca2+ channels in apical dendrites of rat CA1 pyramidal neurons. Journal of Physiology 487, 67–90. [PubMed: 7473260]

Maghsoodi B, Poon MM, Nam CI, Aoto J, Ting P, and Chen L (2008). Retinoic acid regulates RARalpha-mediated control of translation in dendritic RNA granules during homeostatic synaptic plasticity. Proc Natl Acad Sci U S A 105, 16015–16020. [PubMed: 18840692]

Malik AN, Vierbuchen T, Hemberg M, Rubin AA, Ling E, Couch CH, Stroud H, Spiegel I, Farh KK, Harmin DA, et al. (2014). Genome-wide identification and characterization of functional neuronal activity-dependent enhancers. Nat Neurosci 17, 1330–1339. [PubMed: 25195102]

Marx M, Gunter RH, Hucko W, Radnikow G, and Feldmeyer D (2012). Improved biocytin labeling and neuronal 3D reconstruction. Nat Protoc 7, 394–407. [PubMed: 22301777]

Mayford M, Baranes D, Podsypanina K, and Kandel ER (1996). The 3'-untranslated region of CaMKII alpha is a cis-acting signal for the localization and translation of mRNA in dendrites. Proc Natl Acad Sci U S A 93, 13250–13255. [PubMed: 8917577]

Mignone F, Gissi C, Liuni S, and Pesole G (2002). Untranslated regions of mRNAs. Genome biology 3, REVIEWS0004.

Nelles DA, Fang MY, O'Connell MR, Xu JL, Markmiller SJ, Doudna JA, and Yeo GW (2016). Programmable RNA Tracking in Live Cells with CRISPR/Cas9. Cell 165, 488–496. [PubMed: 26997482]

Neph S, Kuehn MS, Reynolds AP, Haugen E, Thurman RE, Johnson AK, Rynes E, Maurano MT, Vierstra J, Thomas S, et al. (2012). BEDOPS: high-performance genomic feature operations. Bioinformatics 28, 1919–1920. [PubMed: 22576172]

O'Connell MR, Oakes BL, Sternberg SH, East-Seletsky A, Kaplan M, and Doudna JA (2014). Programmable RNA recognition and cleavage by CRISPR/Cas9. Nature 516, 263–266. [PubMed: 25274302]

Okuno H, Akashi K, Ishii Y, Yagishita-Kyo N, Suzuki K, Nonaka M, Kawashima T, Fujii H, Takemoto-Kimura S, Abe M, et al. (2012). Inverse synaptic tagging of inactive synapses via dynamic interaction of Arc/Arg3.1 with CaMKIIbeta. Cell 149, 886–898. [PubMed: 22579289]

Ooe N, Saito K, and Kaneko H (2009). Characterization of functional heterodimer partners in brain for a bHLH-PAS factor NXF. Biochimica et biophysica acta 1789, 192–197. [PubMed: 19284974]

Ooe N, Saito K, Mikami N, Nakatuka I, and Kaneko H (2004). Identification of a novel basic helix-loop-helix-PAS factor, NXF, reveals a Sim2 competitive, positive regulatory role in dendritic-cytoskeleton modulator drebrin gene expression. Mol Cell Biol 24, 608–616. [PubMed: 14701734]

Perreault P, Tancredi V, and Avoli M (1989). Failure of the antiepileptic drug valproic acid to modify synaptic and non-synaptic responses of CA1 hippocampal pyramidal cells maintained 'in vitro'. Epilepsy Res 3, 227–231. [PubMed: 2499451]

Pevzner A, Miyashita T, Schiffman AJ, and Guzowski JF (2012). Temporal dynamics of Arc gene induction in hippocampus: relationship to context memory formation. Neurobiol Learn Mem 97, 313–320. [PubMed: 22390855]

Pologruto TA, Sabatini BL, and Svoboda K (2003). ScanImage: flexible software for operating laser scanning microscopes. Biomed Eng Online 2, 13. [PubMed: 12801419]

Rada-Iglesias A, Bajpai R, Swigut T, Brugmann SA, Flynn RA, and Wysocka J (2011). A unique chromatin signature uncovers early developmental enhancers in humans. Nature 470, 279–283. [PubMed: 21160473]

Ramachandran KV, Fu JM, Schaffer TB, Na CH, Delannoy M, and Margolis SS (2018). Activity-Dependent Degradation of the Nascentome by the Neuronal Membrane Proteasome. Mol Cell 71, 169–177 e166. [PubMed: 29979964]

Ramamoorthi K, Fropf R, Belfort GM, Fitzmaurice HL, McKinney RM, Neve RL, Otto T, and Lin Y (2011). Npas4 regulates a transcriptional program in CA3 required for contextual memory formation. Science 334, 1669–1675. [PubMed: 22194569]

Ramirez F, Dundar F, Diehl S, Gruning BA, and Manke T (2014). deepTools: a flexible platform for exploring deep-sequencing data. Nucleic Acids Res 42, W187–191. [PubMed: 24799436]

Ran FA, Hsu PD, Wright J, Agarwala V, Scott DA, and Zhang F (2013). Genome engineering using the CRISPR-Cas9 system. Nat Protoc 8, 2281–2308. [PubMed: 24157548]

Renier N, Adams EL, Kirst C, Wu Z, Azevedo R, Kohl J, Autry AE, Kadiri L, Umadevi Venkataraju K, Zhou Y, et al. (2016). Mapping of Brain Activity by Automated Volume Analysis of Immediate Early Genes. Cell 165, 1789–1802. [PubMed: 27238021]

Reuter JS, and Mathews DH (2010). RNAstructure: software for RNA secondary structure prediction and analysis. BMC bioinformatics 11, 129. [PubMed: 20230624]

Rubio A, Luoni M, Giannelli SG, Radice I, Iannielli A, Cancellieri C, Di Berardino C, Regalia G, Lazzari G, Menegon A, et al. (2016). Rapid and efficient CRISPR/Cas9 gene inactivation in human neurons during human pluripotent stem cell differentiation and direct reprogramming. Sci Rep 6, 37540. [PubMed: 27857203]

Saha RN, Wissink EM, Bailey ER, Zhao M, Fargo DC, Hwang JY, Daigle KR, Fenn JD, Adelman K, and Dudek SM (2011). Rapid activity-induced transcription of Arc and other IEGs relies on poised RNA polymerase II. Nat Neurosci 14, 848–856. [PubMed: 21623364]

Schindelin J, Arganda-Carreras I, Frise E, Kaynig V, Longair M, Pietzsch T, Preibisch S, Rueden C, Saalfeld S, Schmid B, et al. (2012). Fiji: an open-source platform for biological-image analysis. Nat Methods 9, 676–682. [PubMed: 22743772]

Schmitz SK, Hjorth JJ, Joemai RM, Wijntjes R, Eijgenraam S, de Bruijn P, Georgiou C, de Jong AP, van Ooyen A, Verhage M, et al. (2011). Automated analysis of neuronal morphology, synapse number and synaptic recruitment. Journal of neuroscience methods 195, 185–193. [PubMed: 21167201]

Schneider CA, Rasband WS, and Eliceiri KW (2012). NIH Image to ImageJ: 25 years of image analysis. Nat Methods 9, 671–675. [PubMed: 22930834]

Sharma N, Pollina EA, Nagy MA, Yap EL, DiBiase FA, Hrvatin S, Hu L, Lin C, and Greenberg ME (2019). ARNT2 Tunes Activity-Dependent Gene Expression through NCoR2-Mediated Repression and NPAS4-Mediated Activation. Neuron 102, 390–406 e399. [PubMed: 30846309]

Sheng M, McFadden G, and Greenberg ME (1990). Membrane depolarization and calcium induce c-fos transcription via phosphorylation of transcription factor CREB. Neuron 4, 571–582. [PubMed: 2157471]

Sommerlandt FMJ, Brockmann A, Rössler W, and Spaethe J (2019). Immediate early genes in social insects: a tool to identify brain regions involved in complex behaviors and molecular processes underlying neuroplasticity. Cell Mol Life Sci 76, 637–651. [PubMed: 30349993]

Spiegel I, Mardinly AR, Gabel HW, Bazinet JE, Couch CH, Tzeng CP, Harmin DA, and Greenberg ME (2014). Npas4 regulates excitatory-inhibitory balance within neural circuits through cell-type-specific gene programs. Cell 157, 1216–1229. [PubMed: 24855953]

Sullivan AE, Peet DJ, and Whitelaw ML (2016). MAGED1 is a novel regulator of a select subset of bHLH PAS transcription factors. FEbS J 283, 3488–3502. [PubMed: 27472814]

Swanson HI, Chan WK, and Bradfield CA (1995). DNA binding specificities and pairing rules of the Ah receptor, ARNT, and SIM proteins. J Biol Chem 270, 26292–26302. [PubMed: 7592839]

Swiech L, Heidenreich M, Banerjee A, Habib N, Li Y, Trombetta J, Sur M, and Zhang F (2015). In vivo interrogation of gene function in the mammalian brain using CRISPR-Cas9. Nat Biotechnol 33, 102–106. [PubMed: 25326897]

Taniguchi H, He M, Wu P, Kim S, Paik R, Sugino K, Kvitsiani D, Fu Y, Lu J, Lin Y, et al. (2011). A resource of Cre driver lines for genetic targeting of GABAergic neurons in cerebral cortex. Neuron 71, 995–1013. [PubMed: 21943598]

tom Dieck S, Kochen L, Hanus C, Heumuller M, Bartnik I, Nassim-Assir B, Merk K, Mosler T, Garg S, Bunse S, et al. (2015). Direct visualization of newly synthesized target proteins in situ. Nat Methods 12, 411–414. [PubMed: 25775042]

Tushev G, Glock C, Heumuller M, Biever A, Jovanovic M, and Schuman EM (2018). Alternative 3' UTRs Modify the Localization, Regulatory Potential, Stability, and Plasticity of mRNAs in Neuronal Compartments. Neuron 98, 495–511 e496. [PubMed: 29656876]

Tyssowski KM, DeStefino NR, Cho JH, Dunn CJ, Poston RG, Carty CE, Jones RD, Chang SM, Romeo P, Wurzelmann MK, et al. (2018). Different Neuronal Activity Patterns Induce Different Gene Expression Programs. Neuron 98, 530–546 e511. [PubMed: 29681534]

Vaccarino FM, Hayward MD, Nestler EJ, Duman RS, and Tallman JF (1992). Differential induction of immediate early genes by excitatory amino acid receptor types in primary cultures of cortical and striatal neurons. Brain Res Mol Brain Res 12, 233–241. [PubMed: 1347632]

Wang F, Flanagan J, Su N, Wang LC, Bui S, Nielson A, Wu X, Vo HT, Ma XJ, and Luo Y (2012). RNAscope: a novel in situ RNA analysis platform for formalin-fixed, paraffin-embedded tissues. The Journal of molecular diagnostics : JMD 14, 22–29. [PubMed: 22166544]

Weng FJ, Garcia RI, Lutzu S, Alvina K, Zhang Y, Dushko M, Ku T, Zemoura K, Rich D, Garcia-Dominguez D, et al. (2018). Npas4 Is a Critical Regulator of Learning-Induced Plasticity at Mossy Fiber-CA3 Synapses during Contextual Memory Formation. Neuron 97, 1137–1152 e1135. [PubMed: 29429933]

West A, Dupre SM, Yu L, Paton IR, Miedzinska K, McNeilly AS, Davis JR, Burt DW, and Loudon AS (2013). Npas4 is activated by melatonin, and drives the clock gene Cry1 in the ovine pars tuberalis. Mol Endocrinol 27, 979–989. [PubMed: 23598442]

Wiegert JS, Bengtson CP, and Bading H (2007). Diffusion and not active transport underlies and limits ERK1/2 synapse-to-nucleus signaling in hippocampal neurons. J Biol Chem 282, 29621–29633. [PubMed: 17675293]

Wild AR, Sinnen BL, Dittmer PJ, Kennedy MJ, Sather WA, and Dell'Acqua ML (2019). Synapse-to-Nucleus Communication through NFAT Is Mediated by L-type Ca(2+) Channel Ca(2+) Spike Propagation to the Soma. Cell reports 26, 3537–3550 e3534. [PubMed: 30917310]

Wu B, Buxbaum AR, Katz ZB, Yoon YJ, and Singer RH (2015). Quantifying Protein-mRNA Interactions in Single Live Cells. Cell 162, 211–220. [PubMed: 26140598]

Wu B, Eliscovich C, Yoon YJ, and Singer RH (2016). Translation dynamics of single mRNAs in live cells and neurons. Science 352, 1430–1435. [PubMed: 27313041]

Zhou Y, Zhou B, Pache L, Chang M, Khodabakhshi AH, Tanaseichuk O, Benner C, and Chanda SK (2019). Metascape provides a biologist-oriented resource for the analysis of systems-level datasets. Nat Commun 10, 1523. [PubMed: 30944313]

Highlights:

- APs and EPSPs induce NPAS4 in CA1 pyramidal neurons through distinct mechanisms.
- EPSPs trigger dendritic translation of *Npas4* mRNAs distinguished by a long 5’ UTR.
- APs and EPSPs induce the formation of distinct NPAS4 heterodimers.
- NPAS4 heterodimers exhibit distinct patterns of DNA binding and gene regulation.

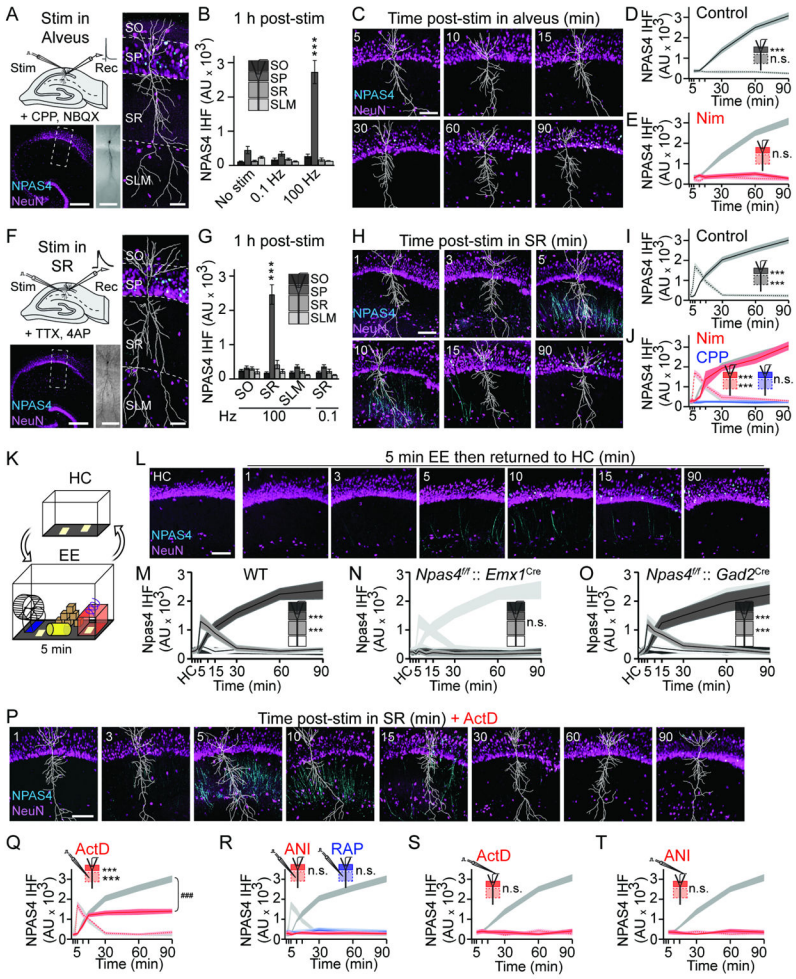

Figure 1. Distinct excitation pathways induce NPAS4 expression in CA1.

A, Schematic of stimulation in alveus. Hippocampal slice (*bottom left*) immunostained for NPAS4 (cyan) and NeuN (magenta). Dashed inset shown at *right*. Biocytin fill (*middle*) and reconstruction (white, *right*) is shown.

B, Quantification of NPAS4 IHF in each layer post-stimulation in alveus.

C, CA1 from slices fixed at the indicated times.

D, Quantification of NPAS4 IHF in SR and SP.

E, As in (D) but with Nim. Data from (D) are replotted in gray.

F, Schematic stimulation in SR (*top left*). Immunostaining as in (A).

G, As in (B) but post-stimulation in SR, SO, or SLM.

H–J, As in (C–E) but post-stimulation in SR. For (J), Nim or CPP in the bath. Data from (I) are replotted in gray.

K, Schematic of EE.

L, CA1 at the indicated times post-EE.

M, Quantification of NPAS4 IHF in CA1 from WT mice at the indicated.

N and **O**, as in (M) but from *Npas4*$^{f/f}$ mice crossed to *Emx1*^{Cre} (**N**) or *Gad2*^{Cre} (**O**) mice.

P, As in (H) but with ActD.

Q and **R**, As in (I) but with ActD (**Q**) and ANI or RAP (**R**). Data from (I) are replotted in gray. SP, 90 min, ActD vs control: $^{###}p<0.001$.

S and **T**, as in (D) but with ActD (**S**) or ANI (**T**). Data from (D) are replotted in gray. Scale bars: (A, F) 300 μm (*bottom left*), 100 μm (*middle*), 50 μm (*right*), and (C, H, L, P) =100 μm. *p<0.05, **p<0.01, ***p<0.001, n.s., not significant. N and statistical tests indexed in Table S1. See also Figures S1 and S2.

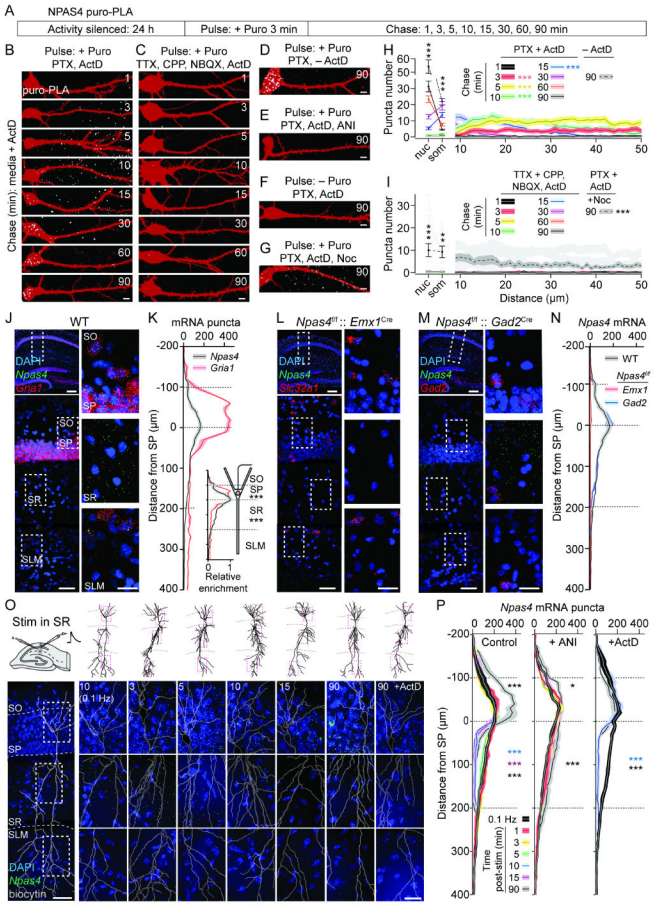

Figure 2. EPSP-induced NPAS4 is translated in dendrites and trafficked to the soma.

A, Schematic of NPAS4 puro-PLA metabolic labeling.

B–**G**, Neurons pulsed then chased for the indicated durations. Newly-synthesized NPAS4 (white) and RFP (red) are shown. Pharmacology as indicated.

H–**I**, Quantification of puro-PLA puncta in the nucleus (nuc), soma (som), and dendrites of neurons. Pharmacology as indicated. Data from (H) replotted in gray (I).

J, smFISH for *Npas4* and *Gria1* mRNAs in hippocampus of WT mice (*top left*). Dashed inset in CA1 is shown (*bottom left* and expanded (*right*).

K, Quantification of mRNA puncta along somato-dendritic axis of CA1. Superficial edge of SP=0 μm. Inset: mRNA normalized to peak in SP.

L and **M**, As in (J) but from *Npas4*$^{f/f}$::*Emx1*^{Cre} (**L**) and *Npas4*$^{f/f}$:: *Gad2*^{Cre} (**M**) mice and probed with *Npas4* and *Slc32a1* or *Gad2*.

N, As in (K), in WT, *Npas4*$^{f/f}$:: *Emx1*^{Cre}, and *Npas4*:.$^{f/f}$::*Gad2*^{Cre} tissue.

O, Schematic of stimulation in SR (*top left*). Images of CA1 probed for *Npas4* at indicated times post-stimulation in SR (*bottom*). Biocytin reconstructions are shown. Dashed insets (*top*; red) are shown (*bottom*).

P, Quantification of *Npas4* puncta at indicated times post-stimulation in SR. Control conditions (*left*), ANI (*middle*) or ActD (*right*) are shown. * denotes significance relative to low frequency stimulation in that layer.

Scale bars: (B–G) 5 μm, (J, L, M) 300 μm (*top left*), (J, L, M, O) 50 μm (*bottom left*), 20 μm (insets). *p<0.05, **p<0.01, ***p<0.001. N and statistical tests indexed in Table S1. See also Figure S3.

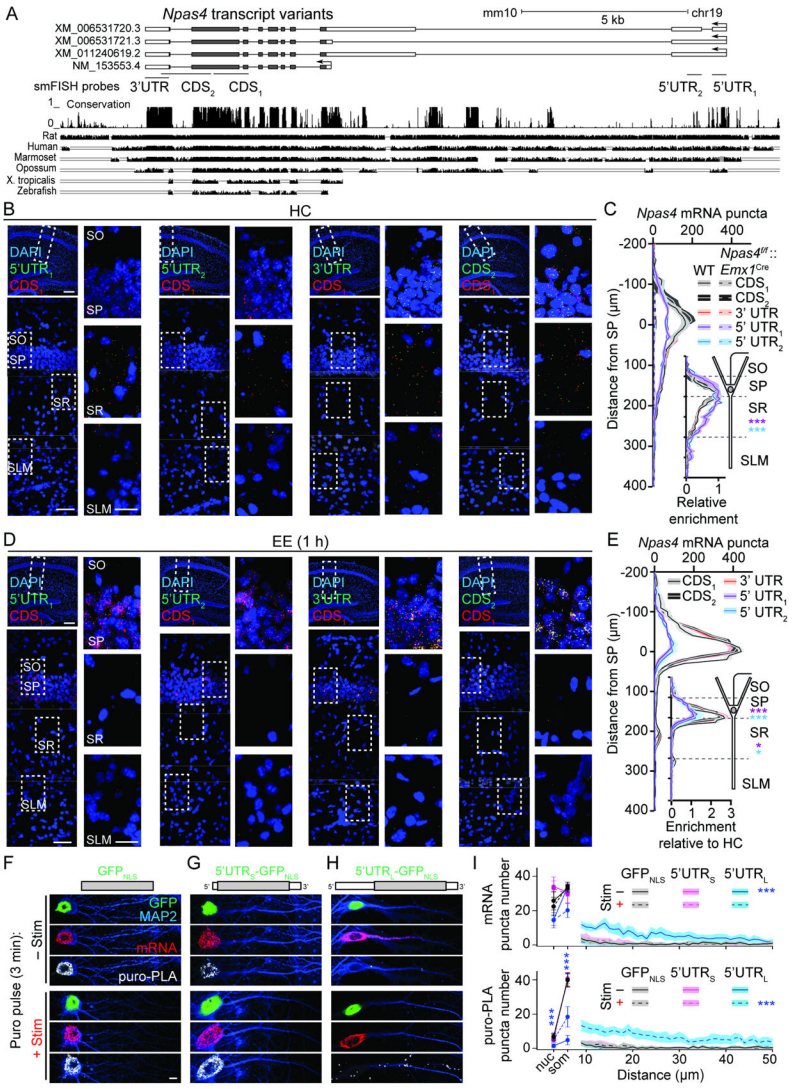

Figure 3. Dendrite-localized *Npas4* mRNAs encompass a long 5' UTR.

A, Predicted (XM_*) and validated (NM_*) transcripts over the *Npas4* locus. Exons: blocks (protein coding, gray; UTRs, white); introns: lines. Regions targeted by smFISH probes (tile exons only; *middle*). PhastCons conservation among vertebrates with examples (*bottom*).

B, smFISH using indicated *Npas4* probes in hippocampal sections from WT mice from HC. Dashed inset is expanded (*right*).

C, Quantification of *Npas4* mRNA puncta in tissue from WT or $Npas4^{f/f}$::Emx^{Cre} mice. Inset: mRNA normalized to peak in SP. * in SR and SP denote significant differences relative to CDS_1.

D, As in (B) but sections from WT mice 1 h post-EE for 5 min.

E, As in (C). Inset: mRNA normalized to peak for respective probe set in HC.

F–H, Neurons transfected with GFP_{NLS} (**F**), 5'UTR_S-GFP_{NLS} (**G**), or 5'UTR_L-GFP_{NLS} (**H**), pulsed with puro plus DMSO (−Stim) or PTX (+Stim) and chased for 15 min. GFP and MAP2 (*top*), smFISH for GFP (*middle*), and puro-PLA for GFP (*bottom*) are shown.

I, Quantification of mRNA (*top*) or puro-PLA puncta (*bottom*) in the nucleus (nuc), soma (som), and dendrites of transfected neurons ± Stim.

Scale bars: (B, D) 300 μm (*top left*), 50 μm (*bottom left*), 20 μm (*insets*), (F–H) 5 μm.

*p<0.05, ***p<0.001. N and statistical tests indexed in Table S1. See also Figure S4.

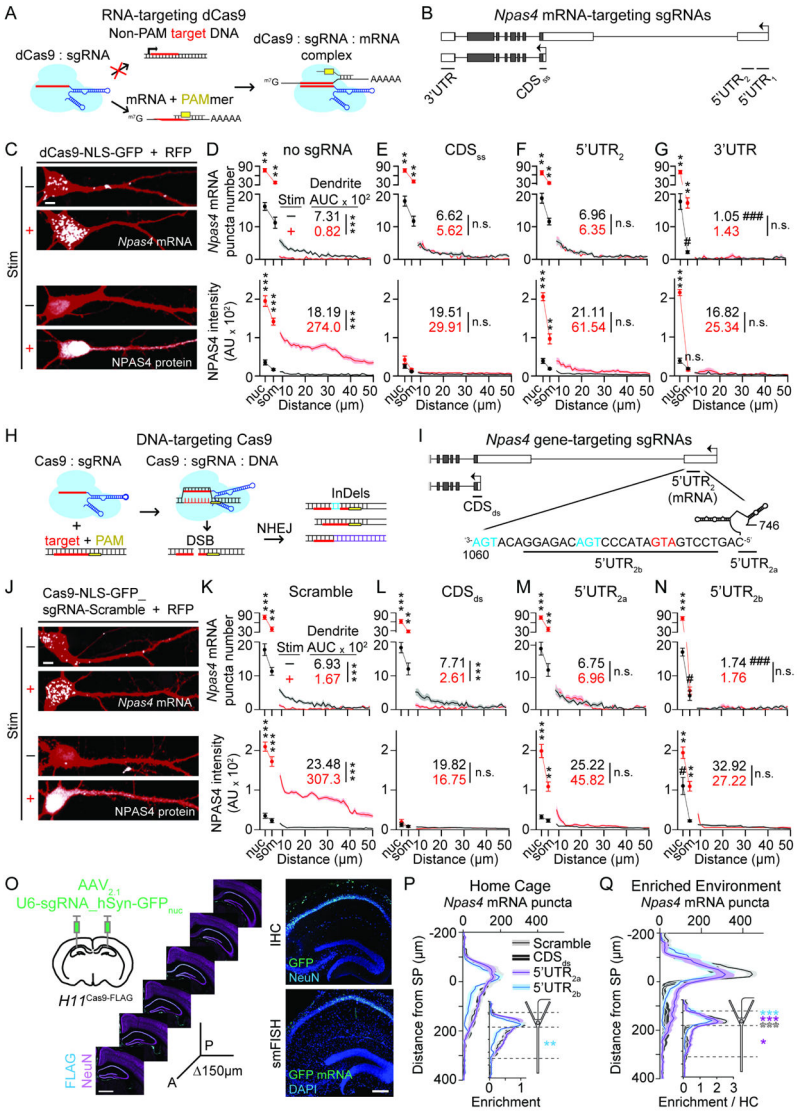

Figure 4. CRISPR manipulation identifies *Npas4* mRNA elements required for dendritic localization and translation.

A, Schematic of RNA-targeting by dCas9 in complex with non-PAM adjacent sgRNA (red); specificity for target mRNA sequences is enhanced by a mismatched DNA/RNA PAMmer (yellow).

B, Schematic of *Npas4* gene and regions targeted by sgRNAs.

C, Neurons co-transfected with dCas9-NLS-GFP and RFP in DMSO (−Stim) or PTX (+Stim) conditions and probed for *Npas4* mRNA (*top*, smFISH CDS_1 or protein (*bottom*).

D–**G**, Quantification of *Npas4* mRNA (*top*) and protein (*bottom*) in the nucleus (nuc), soma (som), and dendrites. Cells co-transfected with dCas9, PAMmer, and the indicated sgRNA.

H, Schematic of DNA-targeting by Cas9 in complex with PAM-adjacent sgRNA (yellow and red). DSB: double strand break; NHEJ: non-homologous end-joining; InDels: insertions/deletions.

I, Schematic of *Npas4* gene and regions targeted by sgRNA. Start codon: red; stop codons: blue.

J, As in (C), but co-transfected with a bi-cistronic construct encoding sgRNA-scramble and Cas9.

K–**N**, As in (D–G), but transfected with the indicated sgRNA.

O, Schematic of AAV injection into **H11**$^{\text{Cas9-FLAG}}$ mice (*left*) and expression of Cas9$^{\text{FLAG}}$ along the anterior (A) – posterior (P) axis (*middle*). Infection was confirmed with immunostaining (*right top*) and smFISH (*bottom right* for GFP.

P–**Q**, Quantification of *Npas4* mRNA in CA1 from *H11*$^{\text{Cas9-FLAG}}$ mice infected with AAV encoding the indicated sgRNAs. Mice housed in HC (P) or 1 h post-EE for 5 min (Q). Inset: mRNA normalized to peak in SP (P) or peak in HC (Q). * in SR and SP denote significant differences relative to sgRNA-scramble.

Scale bars: (C, J) 5 μm, (O) 1 mm (*left*) 300 μm (*right*). *p<0.05, **p<0.01 ***p<0.001, #p<0.05, ###p<0.001 relative to control −Stim cells. N and statistical tests indexed in Table S1. See also Figure S5.

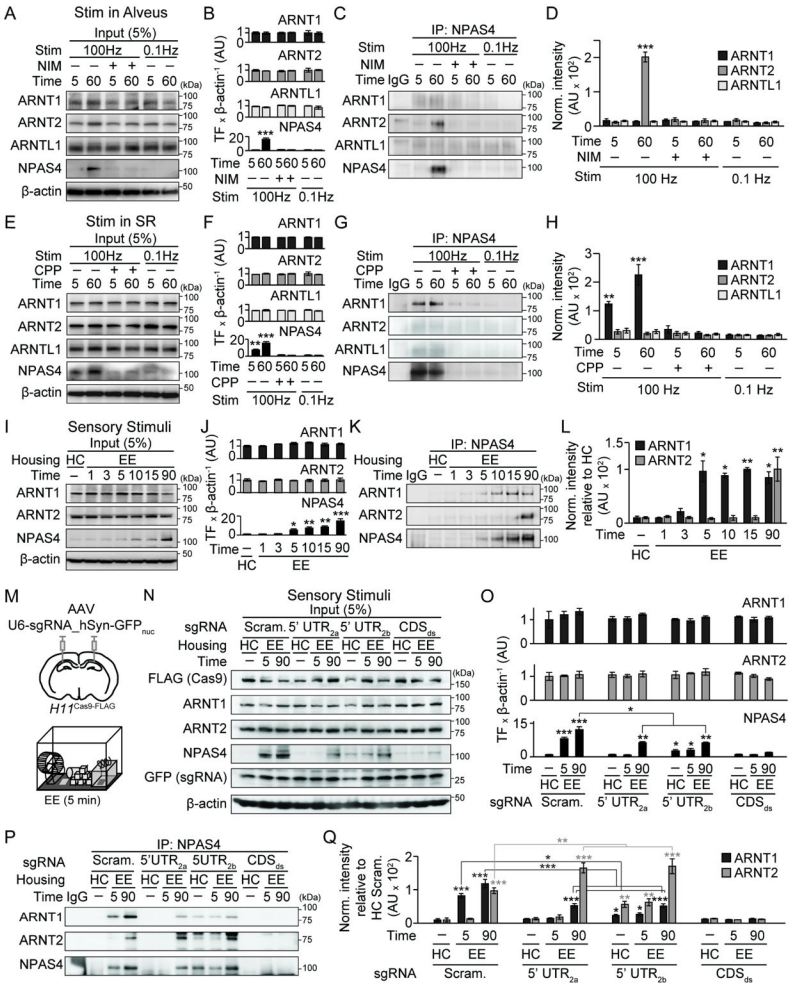

Figure 5. NPAS4 forms excitation pathway-specific heterodimers.

A–**D**, Stimulation in the alveus.

A, WB analysis of ARNT1, ARNT2, ARNTL1, NPAS4, and β-actin from CA1 lysates. Stimulation, pharmacology, and time post-stimulation are indicated.

B, Quantification of TF expression normalized to β-actin.

C, Co-IP of NPAS4 with ARNT1, ARNT2, or ARNTL1 from lysates in (A).

D, Quantification of Co-IP normalized to IgG.

E–**H**, As in (A–D) but with stimulation in SR.

I–**L**, As in (A–D) but hippocampal lysates from WT mice in HC or indicated times post-EE for 5 min.

M, Schematic of injection of AAV into *H11*$^{\text{Cas9-FLAG}}$ mice and EE.

N–**Q**, As in (I–L) but from *H11*$^{\text{Cas9-FLAG}}$ mice infected with the indicated AAV-sgRNA. Housing and time post-EE is indicated.

*p<0.05, **p<0.01 ***p<0.001. N and statistical tests indexed in Table S1. See also Figure S6.

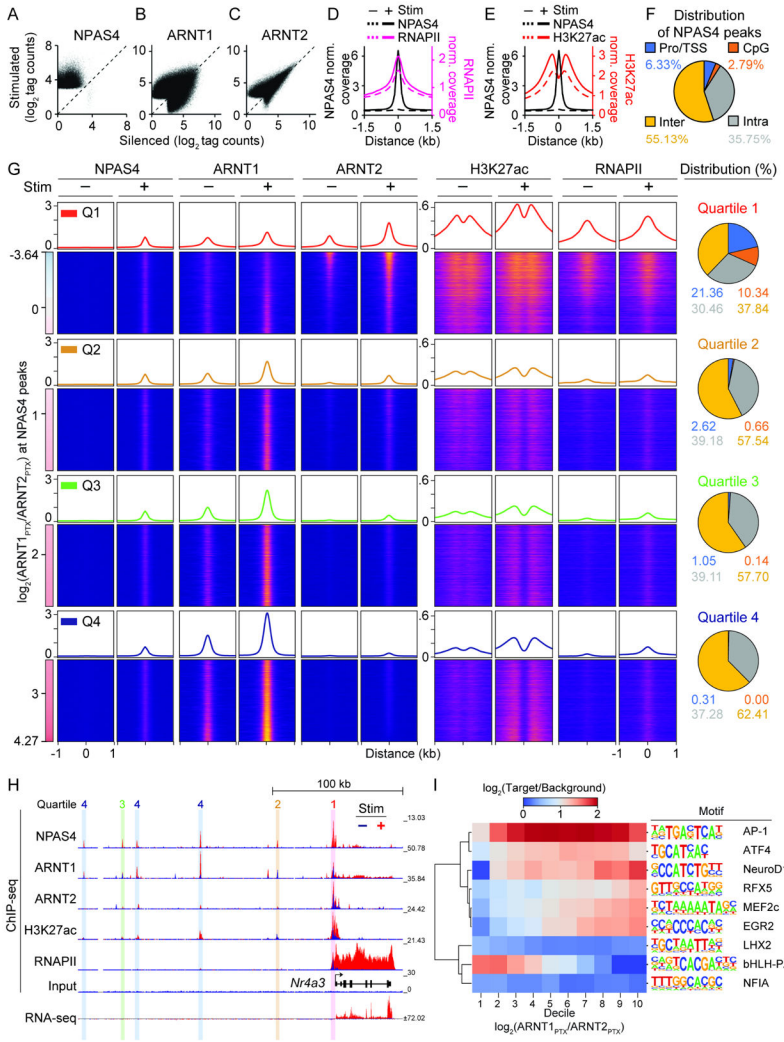

Figure 6. NPAS4 heterodimers exhibit different patterns of DNA binding.

A, Scatter plot of NPAS4 peaks in stimulated (PTX, 2 h) vs silenced (TTX, NBQX, CPP; 24 h) neurons.

B and **C**, As in (A) but for ARNT1 (**B**) or ARNT2 (**C**).

D and **E**, Aggregate plot of NPAS4 and RNAPII (**D**) or H3K27ac (**E**) peaks as a function of distance from NPAS4 peak center in silenced and stimulated neurons.

F, Distribution of NPAS4 peaks at promoters/TSS, CpG-rich, intra-, and intergenic sites.

G, NPAS4, ARNT1, ARNT2, H3K27ac, RNAPII peaks sorted along the continuum of ARNT1 and ARNT2 co-binding in stimulated neurons ($\log_2(ARNT1_{PTX}/ARNT2_{PTX})$). Quartiles (Q1–4) span from highest co-bound ARNT2 (*top*; Q1) to highest co-bound ARNT1 (*bottom*; Q4). Aggregate plots of normalized coverage are shown above heat maps. Distribution of NPAS4 peaks at the indicated genomic loci is shown (*right*).

H, Example tracks for ChIP- and RNA-seq data at the *Nr4a3* locus in silenced (−; blue) and stimulated (+; red) neurons. Vertical bars over peaks denote assigned quartile.

I, Dendrogram and heatmap of motif enrichment of top-ranked *de novo* motifs across deciles of the ARNT1:ARNT2 tag count ratio at NPAS4 peaks in stimulated cells.

See also Figure S7 and Tables S2-S6.

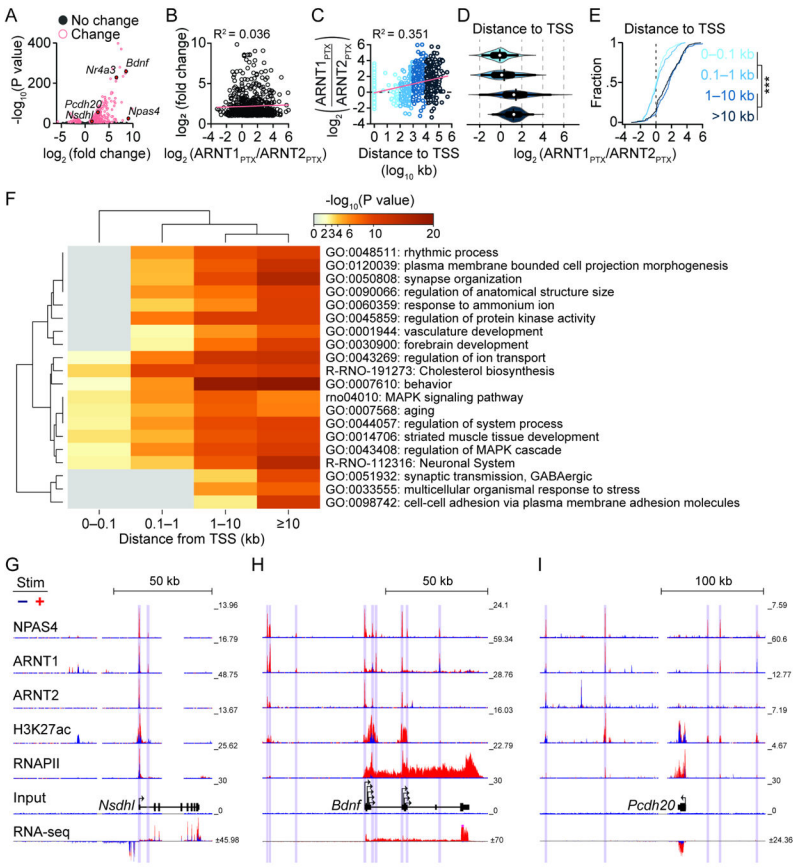

Figure 7. NPAS4 heterodimers are recruited to distinct regions of activity-upregulated genes.

A, Volcano plot of change in gene expression between silenced and stimulated neurons. Activity-regulated genes (pink): fold change ≥2 and $-\log_{10}$(P value)>5.

B, Scatter plot of upregulated genes vs. $\log_2(ARNT1_{PTX}/ARNT2_{PTX})$ from the NPAS4 peak nearest the TSS of the activity-regulated gene.

C, Scatter plot depicting $\log_2(ARNT1_{PTX}/ARNT2_{PTX})$ vs. distance of NPAS4 to TSS of an activity-induced gene.

D, Violin plot of $\log_2(ARNT1_{PTX}/ARNT2_{PTX})$ values at NPAS4 peaks assigned to the nearest activity-upregulated gene and binned by distance. Mean: vertical bar, median: white circle, SEM: thick horizontal bar, SD: thin horizontal bar, and distribution: colored contour.

E, Cumulative fraction of $\log_2$ $(ARNT1_{PTX}/ARNT2_{PTX})$ values at NPAS4 peaks assigned to the nearest activity-upregulated gene and binned by distance from TSS. ***p<0.0001.

F, Metascape heatmap and dendrogram of GO term enrichment among upregulated genes with NPAS4 peaks at increasing distance from TSS.

G–I, Example ChIP- and RNA-seq tracks at genes with NPAS4 peaks at the TSS (*Nsdhl*, **G**), TSS and distal sites (*Bdnf*, **H**) and distal only sites (*Pcdh20*, **I**). Vertical bars denote called peaks.

(B, C) Linear regression (pink) and R^2 values. See also Table S6.

KEY RESOURCES TABLE

REAGENT or RESOURCE	SOURCE	IDENTIFIER
Antibodies		
Rabbit polyclonal anti-NPAS4 (used in IHC and biochemistry experiments)	M.E. Greenberg, Harvard Medical School	Lin et al., 2008; RRID:AB_2687869
Rabbit monoclonal anti-NPAS4 (clone 92-3; used in ChIP-seq experiments)	DART Neuroscience	N/A
Guinea pig polyclonal anti-NeuN	Synaptic Systems	Cat#266 004; RRID:AB_2619988
Mouse monoclonal anti-ARNT1 (Hif1b; clone 2B10, used for IHC and biochemistry experiments)	ThermoFisher Scientific	Cat#MA1-515; RRID:AB_2059441
Rabbit monoclonal anti-ARNT1 (clone D28F3; used for ChIP-seq experiments)	Cell Signaling Technology	Cat#5537; RRID:AB_10694232
Rabbit polyclonal anti-H3K27ac	Active Motif	Cat#39133; RRID:AB_2561016
Rabbit polyclonal anti-RPB2 N-terminus (RNAPII)	Genetex	Cat#GTX102535; RRID:AB_1951313
Mouse monoclonal anti-ARNT2 (clone B11)	Santa Cruz Biotechnology	Cat#sc-3936 RRID:AB_2783034
Mouse monoclonal anti-ARNTL1 (clone B-1)	Santa Cruz Biotechnology	Cat#sc-365645; RRID:AB_10841724
Mouse monoclonal anti-β-actin (clone AC-15)	Sigma Aldrich	Cat#A1978; RRID:AB_476692
Rabbit polyclonal anti-GFP (used in RNA-IP experiments)	Synaptic Systems	Cat#132002; RRID:AB_887725
Chicken polyclonal anti-GFP (used in IHC and ICC experiments	ThermoFisher Scientific	Cat#A10262; RRID:AB_2534023
Mouse monoclonal anti-FLAG (M2 clone)	Sigma Aldrich	Cat#F1365; RRID:AB_259529
Rabbit polyclonal anti-RFP	Abcam	Cat#ab62341; RRID:AB_945213
Rabbit polyclonal anti-GFP (used in Puro-PLA experiments)	Abcam	Cat#ab290; RRID:AB_303395
Mouse monoclonal anti-Puromycin	Kerafast	Cat#EQ0001, RRID:AB_2620162
Guinea pig polyclonal anti-MAP2	Synaptic Systems	Cat# 188 004, RRID:AB_2138181
Normal rabbit IgG	Santa Cruz Biotechnology	Cat#sc-2027; RRID:AB_737197
Goat anti-mouse AlexaFluor 405	ThermoFisher Scientific	Cat#A-31553; RRID:AB_221604
Goat anti-rabbit AlexaFluor 488	ThermoFisher Scientific	Cat#A-11008; RRID:AB_143165
Goat anti-rabbit AlexaFluor 568	ThermoFisher Scientific	Cat#A-11011; RRID:AB_143157
Goat anti-guinea pig AlexaFluor 647	ThermoFisher Scientific	Cat#A-21450; RRID:AB_2735091
Goat anti-chicken AlexaFluor 488	ThermoFisher Scientific	Cat#A-11039; RRID:AB_2534096
Goat anti-rabbit AlexaFluor 647	ThermoFisher Scientific	Cat#A-21244; RRID:AB_2535812
Goat anti-mouse IgG-HRP	BioRad Inc.	Cat#1721011; RRID:AB_11125936

REAGENT or RESOURCE	SOURCE	IDENTIFIER
Goat anti-rabbit IgG-HRP	BioRad Inc.	Cat#1706515; RRID:AB_11125142
Bacterial and Virus Strains		
$AAV_{2.1}$_U6-sgRNA-Scramble_hSyn-GFP_{nuc}	This paper	N/A
$AAV_{2.1}$_U6-sgRNA-CDS_{ds}_hSyn-GFP_{nuc}	This paper	N/A
$AAV_{2.1}$_U6-sgRNA-5'UTR_{2a}_hSyn-GFP_{nuc}	This paper	N/A
$AAV_{2.1}$_U6-sgRNA-5'UTR_{2b}_hSyn-GFP_{nuc}	This paper	N/A
Chemicals, Peptides, and Recombinant Proteins		
Kynurenic acid (KYN)	Tocris Bioscience	Cat#0223
Tetrodotoxin Citrate (TTX)	Tocris Bioscience	Cat#1069
4-Aminopyridine (4AP)	Sigma Aldrich	Cat#275875
3-((R)-2-Carboxypiperazin-4-yl)-propyl-1-phosphonic acid (CPP)	Tocris Bioscience	Cat#0247
2,3-Dioxo-6-nitro-1,2,3,4-tetrahydrobenzo[f]quinoxaline-7-sulfonamide disodium salt (NBQX)	Tocris Bioscience	Cat#1044
Nimodipine (NIM)	Tocris Bioscience	Cat#0600
Anisomycin (ANI)	Tocris Bioscience	Cat#1290
Actinomycin D (ActD)	Tocris Bioscience	Cat#1229
Nocodazole (Noc)	Tocris Bioscience	Cat#1228
Rapamycin (RAP)	Tocris Bioscience	Cat#1292
Colchicine (Colch)	Tocris Bioscience	Cat#1364
Picrotoxin (PTX)	Tocris Bioscience	Cat#1128
Triton X-100	Sigma Aldrich	Cat#9410-OP
N-Lauroylsarcosine	Sigma Aldrich	Cat#L7414
Sodium Dexycholate	Sigma Aldrich	Cat#30970
Proteinase K (20 mg/ml)	ThermoFisher Scientific	Cat#AM2548
PEG 8000	Fisher BioReagents	Cat#BP233-1
Tween 20 (10%)	ThermoFisher Scientific	Cat#28320
Puromycin dihydrochloride from Streptomyces alboniger	Sigma Aldrich	Cat#P8833
Critical Commercial Assays		
RNAscope® Fluorescent Multiplex Kit	ACD bio / Bio-Techne	Cat#320850
RNAscope® Target Retrieval Reagents	ACD bio / Bio-Techne	Cat#322000
Standard Ultra-Sensitive ABC Staining Kit	ThermoFisher Scientific	Cat#32050
Imprint® RNA Immunoprecipitation Kit	Sigma Aldrich	Cat#RIP-12RXN
NEBnext Ultra II DNA Library Prep Kit for Illumina	New England BioLabs	Cat#E7645S
NEXTflex DNA Barcodes - 48	Bioo Scientific	Cat#NOVA-514104
Duolink® In Situ PLA® Probe Anti-Rabbit PLUS	Sigma Aldrich	Cat#DUO92002
Duolink® In Situ PLA® Probe Anti-Mouse MINUS	Sigma Aldrich	Cat#DUO92004
Duolink® In Situ Detection Reagents FarRed	Sigma Aldrich	Cat#DUO92013
Duolink® In Situ Wash Buffers, Fluorescence	Sigma Aldrich	Cat#DUO82049
Direct-Zol RNA miniprep kit	Zymo Research	Cat#R2051

REAGENT or RESOURCE	SOURCE	IDENTIFIER
Deposited Data		
ChIP-seq Data	This Paper	NCBI GSE127793
RNA-seq Data	This Paper	NCBI GSE134203
Experimental Models: Cell Lines		
HEK293T cells	ATCC	Cat#ATCC® CRL-3216™; RRID:CVCL_0063
Primary hippocampal neuron cultures derived from postnatal day 0 Sprague-Dawley rat pups	Rats obtained from: Charles River	RGD Cat# 734476, RRID:RGD_734476
Experimental Models: Organisms/Strains		
Mouse: Wildtype (WT; C57BL/6J)	The Jackson Laboratory	Cat#JAX000664; RRID:IMSR_JAX:00 0664
Mouse: *Npas4*$^{-/-}$	M.E. Greenberg, Harvard Medical School, Boston MA	Lin et al., 2008
Mouse: *Npas4*$^{f/f}$	M.E. Greenberg, Harvard Medical School, Boston MA	Lin et al., 2008
Mouse: *Emx1*^{Cre}	The Jackson Laboratory	Cat#JAX005628; RRID:IMSR_JAX:00 5628
Mouse: *Gad2*^{Cre}	The Jackson Laboratory	Cat#JAX010802; RRID:IMSR_JAX:01 0802
Mouse: *Thy1*^{GFP}	The Jackson Laboratory	Cat#JAX011070; RRID:IMSR_JAX:01 1070
Mouse: *H11*$^{Cas9\text{-}FLAG}$	The Jackson Laboratory	Cat#JAX027650; RRID:IMSR_JAX:02 7650
Oligonucleotides		
Target, sgRNA, and PAMmer sequences for dCas9 recruitment to mRNA, related to Figure 4; See Table S7.	This paper	N/A
Target and sgRNA sequences for Cas9 editing of DNA, related to Figure 4; See Table S7.	This paper	N/A
Target and sgRNA sequences for AAV infection of H11$^{Cas9\text{-}Flag}$ mice, related to Figures 4 and 5; **See** Table S7.	This paper	N/A
Target and sgRNA sequences for Cas9 editing of DNA, related to Figure S5; See Table S7.	This paper	N/A
Npas4 and *Actb* primers used in RNA-IP and T7 endonuclease experiments, related to Figure S5; **See** Table S7.	This paper	N/A
Solexa 1GA primer (used in ChIP—seq library amplification): AATGATACGGCGACCACCGA	This paper	N/A
Solexa 1GB primer (used in ChIP—seq library amplification): CAAGCAGAAGACGGCATACGA	This paper	N/A
Recombinant DNA		
Plasmid: pCDNA3.1- dCas9-2xNLS-EGFP	Nelles et al., 2016	Addgene Cat#74710; RRID: Addgene_74710
Plasmid: RFP (pRP[Exp]-CAG>TurboRFP)	This Paper	N/A
Plasmid: FL-Npas4 (pRP[Exp]-CMV>rNpas4_5'UTR:rNpas4[XM_017588841.1]/HA:rNpas4_3'UTR)	This Paper	N/A
Plasmid: sgRNA λ2 (pRP[Exp]-U6>Target λ2[gRNA]-CAG>TurboRFP)	This Paper	N/A
Plasmid: sgRNA-5'UTR$_1$ (pRP[Exp]-U6>Target 5'UTR$_1$[gRNA]-CAG>TurboRFP)	This Paper	N/A

REAGENT or RESOURCE	SOURCE	IDENTIFIER
Plasmid: sgRNA-5'UTR$_2$ (pRP[Exp]-U6>Target 5'UTR$_2$[gRNA]-CAG>TurboRFP)	This Paper	N/A
Plasmid: sgRNA-CDS$_{ss}$ (pRP[Exp]-U6>Target CDS$_{ss}$[gRNA]-CAG>TurboRFP)	This Paper	N/A
Plasmid: sgRNA-3'UTR (pRP[Exp]-U6>Target 3'UTR[gRNA]-CAG>TurboRFP)	This Paper	N/A
Plasmid: pSpCas9(BB)-2A-GFP (PX458)	Ran et al., 2013	Addgene Cat#48138; RRID: Addgene_48138
Plasmid: sgRNA-Scramble_Cas9-GFP	This Paper	N/A
Plasmid: sgRNA-CDS$_{ds}$_Cas9-GFP	This Paper	N/A
Plasmid: sgRNA-5'UTR$_{2a}$_Cas9-GFP	This Paper	N/A
Plasmid: sgRNA-5'UTR$_{2b}$_Cas9-GFP	This Paper	N/A
pAAV_U6-sgRNA_hSyn-GFP$_{nuc}$ vector (pAAV-U6sgRNA(SapI)_hSyn-GFP-KASH-bGH (PX552))	Sweich et al., 2014	Addgene Cat#60958; RRID:Addgene_609 58
Plasmid: GFP$_{NLS}$ (pRP[Exp]-CMV>EGFP/3xNLS)	This Paper	N/A
Plasmid: 5'UTR$_S$-GFP$_{NLS}$ (pRP[Exp]-CMV>{rNpas4_S5UTR}:EGFP/3xNLS:{rNpas4_3UTR})	This Paper	N/A
Plasmid: 5'UTR$_L$-GFP$_{NLS}$ (pRP[Exp]-CMV>{rNpas4_L5UTR}:EGFP/3xNLS:{rNpas4_3UTR})	This Paper	N/A
Plasmid: 2xsgRNA-ARNT2-CDS_Cas9-GFP$_{NLS}$ (pRP[2CRISPR]-EGFP-hCas9-U6>{ARNT2_CDS1}-U6>{ARNT2_CDS2})	This Paper	N/A
Plasmid: 2xsgRNA-ARNT1-CDS_Cas9-GFP$_{NLS}$ (pRP[2CRISPR]-EGFP-hCas9-U6>{ARNT1_CDS1}-U6>{ARNT1_CDS2})	This Paper	N/A
Software and Algorithms		
FASTP	Chen et al., 2018	https://github.com/OpenGene/fastp
Bowtie2	Langmead and Salzberg, 2012	http://bowtie-bio.sourceforge.net/bowtie2/index.shtml
deepTools	Ramirez et al., 2014	http://deeptools.ie-freiburg.mpg.de
SAMtools	Li et al., 2009	http://samtools.sourceforge.net
STAR	Dobin et al., 2013	http://code.google.com/p/rna-star/
DESeq2	Love et al., 2014	https://bioconductor.org/packages/release/bioc/html/DESeq2.html
Metascape	Zhou et al., 2019	https://metascape.org
BEDOPS	Neph et al., 2012	http://code.google.com/p/bedops/
Seaborn	Waskom et al., 2018	https://github.com/mwaskom/seaborn/tree/v0.9.0
PhastCons	Felsenstein et al., 1996	http://genome.ucsc.edu
HOMER	Heinz et al., 2010	http://homer.ucsd.edu/homer/
UCSC Genome Browser	Bailey et al., 2002; Kent et al., 2002	http://genome.ucsc.edu
Matlab (R2009b)	Mathworks Inc.	https://www.mathworks.com/

REAGENT or RESOURCE	SOURCE	IDENTIFIER
ScanImage	Pologruto et al., 2003	http://scanimage.vidriotechnologies.com
Igor Pro	WaveMetrics	https://www.wavemetrics.com/
Fiji	Schindelin et al., 2012	http://fiji.sc
ImageJ	Schneider et al., 2012	http://imagej.net
SynD	Schmitz et al., 2011	https://www.johanneshjorth.se/SynD/SynD.html
Photoshop CC	Adobe Systems Inc.	https://www.adobe.com/Photoshop
Illustrator CC	Adobe Systems Inc.	https://www.adobe.com/products/illustrator
Prism	GraphPad Inc.	https://www.graphpad.com/scientific-software/prism/
Other		
DAPI (4′,6-diamidino-2-phenylindole)	ACD bio / Bio-Techne	Cat#320858
smFISH probe: Npas4 CDS_1 (probe region: 793 – 1795 (Accession No. NM_153553.4))	ACD bio / Bio-Techne	Cat#423431
smFISH probe: Npas4 CDS_2 (probe region: 1860 – 3067 (Accession No. NM_153553.4))	ACD bio / Bio-Techne	Cat#461631
smFISH probe: Npas4 5'UTR_1 (probe region: 2 – 481 (Accession No. XM_011248619.2))	ACD bio / Bio-Techne	Cat#502521-C3
smFISH probe: Npas4 5'UTR_2 (probe region: 701 – 1166 (Accession No. XM_011248619.2))	ACD bio / Bio-Techne	Cat#502531-C3
smFISH probe: Npas4 3'UTR (probe region: 6801 – 7466 (Accession No. XM_011248619.2))	ACD bio / Bio-Techne	Cat#502351-C3
smFISH probe: Gria1 (probe region 731 – 1700 (Accession No. NM_001113325.2))	ACD bio / Bio-Techne	Cat#426241-C2
smFISH probe: CamKIIα (probe region 896 – 1986 (Accession No. NM_009792.3))	ACD bio / Bio-Techne	Cat#445231
smFISH probe: Arnt1 (probe region 1024 – 1941 (Accession No. NM_001037737.2))	ACD bio / Bio-Techne	Cat#457301-C2
smFISH probe: Arnt2 (probe region 2512 – 3561 (Accession No. NM_007488.3))	ACD bio / Bio-Techne	Cat#457311-C2
smFISH probe: Slc32a1 (probe region 894 – 2037 (Accession No. NM_009508.2))	ACD bio / Bio-Techne	Cat#319191-C3
smFISH probe: Gad2 (probe region 552 – 1506 (Accession No. NM_008078.2))	ACD bio / Bio-Techne	Cat#415071-C2
smFISH probe: Fos (probe region 443 – 1447 (Accession No. NM_010234.2))	ACD bio / Bio-Techne	Cat#316921-C2
smFISH probe: GFP (probe region 628 – 1352 (Accession No. U55763.1))	ACD bio / Bio-Techne	Cat#400281-C2